CONF-9705115
ORNL/FMP-97/1

U.S. Department of Energy
Fossil Energy
Advanced Research and Technology Development

Proceedings of the Eleventh Annual Conference On Fossil Energy Materials

May 20-22, 1997
Knoxville, Tennessee

Fossil Energy AR&TD Materials Program

OAK RIDGE NATIONAL LABORATORY
MANAGED BY
LOCKHEED MARTIN ENERGY RESEARCH CORP.
FOR THE
U.S. DEPARTMENT OF ENERGY
UNDER CONTRACT DE-AC05-96OR22464

Fossil
Energy
Program

CONF-9705115
ORNL/FMP-97/1

PROCEEDINGS OF THE ELEVENTH ANNUAL CONFERENCE ON FOSSIL ENERGY MATERIALS

May 20-22, 1997
Knoxville, Tennessee

Compiled by
R. R. Judkins

Date Published: December 1997

Prepared by the
Department of Energy
Fossil Energy Office of Advanced Research
and
Oak Ridge Operations Office
AA 15 10 10 0

Prepared by the
OAK RIDGE NATIONAL LABORATORY
Oak Ridge, Tennessee 37831-6285
managed by
LOCKHEED MARTIN ENERGY RESEARCH CORP.
for the
U. S. DEPARTMENT OF ENERGY
under Contract DE-AC05-96OR22464

PREFACE

The Eleventh Annual Conference on Fossil Energy Materials was held in Knoxville, Tennessee, on May 20-22, 1997. The meeting was sponsored by the U.S. Department of Energy's (DOE) Office of Fossil Energy through the Advanced Research and Technology Development (AR&TD) Materials Program. The objective of the AR&TD Materials Program is to conduct research and development on materials for longer-term fossil energy applications as well as for generic needs of various fossil fuel technologies. The management of the program has been decentralized to the DOE Oak Ridge Operations Office and Oak Ridge National Laboratory (ORNL). The research is performed by staff members at ORNL and by researchers at other national laboratories, universities, and in private industry. The work is divided into the following categories: (1) structural ceramics, (2) new alloys and coatings, (3) functional materials, and (4) technology development and transfer.

This conference is held each year to review the work on all of the projects of the program. The final program for the meeting is given in Appendix A, and a list of attendees is presented in Appendix B.

These proceedings have been published from camera-ready masters supplied by the authors. All of the contributions have been checked for errors but have not been subjected to peer reviews. However, most of the papers have already undergone technical review within the individual organizations before submission to the Program Office.

The successful completion of the conference and publication of the proceedings has required help from several people. The organizers with to thank Judy Fair for her superb coordination work; Gloria Donaldson and Judy for their excellent work at the registration desk; Thelma Garrett for her help in the many arrangements; and the numerous staff and support personnel associated with the conference. Finally, we express our sincere appreciation to the authors whose efforts are the very basis of the conference.

TABLE OF CONTENTS

SESSION I - CERAMIC COMPOSITES AND FUNCTIONAL MATERIALS

SESSION II - CERAMICS, NEW ALLOYS, AND FUNCTIONAL MATERIALS

SESSION III - WORKSHOP

SESSION IV - NEW ALLOYS

SESSION I

CERAMIC COMPOSITES AND FUNCTIONAL MATERIALS

FABRICATION OF FIBER-REINFORCED COMPOSITES BY CHEMICAL VAPOR INFILTRATION

T. M. Besmann and J. C. McLaughlin
Metals and Ceramics Division
Oak Ridge National Laboratory
P.O. Box 2008, Oak Ridge, TN 37831-6063
e-mail: tmb@ornl.gov

K. J. Probst and T. J. Anderson
Department of Chemical Engineering
University of Florida
Gainesville, FL 32611

T. L. Starr
Department of Materials Science and Engineering
Georgia Institute of Technology
Atlanta, GA 30332-0245

ABSTRACT

Silicon carbide-based heat exchanger tubes are of interest to energy production and conversion systems due to their excellent high temperature properties. Fiber-reinforced SiC is of particular importance for these applications since it is substantially tougher than monolithic SiC, and therefore more damage and thermal shock tolerant. This paper reviews a program to develop a scaled-up system for the chemical vapor infiltration of tubular shapes of fiber-reinforced SiC. The efforts include producing a unique furnace design, extensive process and system modeling, and experimental efforts to demonstrate tube fabrication.

INTRODUCTION

Fiber-reinforced SiC-matrix composites are candidates for a number of high temperature applications due to their high-temperature strength, high thermal conductivity, light weight, thermal shock resistance, creep resistance, and damage tolerance. However, in the current commercial isothermal, isobaric chemical vapor infiltration process, thick-walled parts are difficult to densify. A leading alternative process is forced chemical vapor infiltration (FCVI).[1,2] In FCVI, a preform is placed in a reactor where one side is heated and the other side is cooled, resulting in a thermal gradient across the preform. The reactant gases are constrained to flow from the cooled to the heated side, undergoing a surface, chemical vapor deposition reaction forming the ceramic matrix and an effluent gas. In the case of SiC deposited from chlorosilanes, the effluent HCl gas, has a poisoning effect on the reaction rate. This poisoning, combined with the depletion of the reactant, tends to retard the deposition rate. However, since the gases are traveling toward the hot side of the preform their temperature increases, resulting in faster deposition rates due to the Arrhenius behavior of the deposition reaction. Control over deposition is thus maintained by using the increase in temperature to offset reactant depletion and effluent gas buildup and poisoning effect.

In the current work, emphasis is on the development of composites with tubular geometries. In order to demonstrate the fabrication of a prototypical tube, the efforts have centered on component diameters approaching 100 mm with a 6.4 mm wall thickness. As a result, a unique furnace system was designed and constructed that facilitates the FCVI of such tubes with lengths of 300 mm. Supporting the developmental effort has been extensive process modeling which has successfully described and aided in the optimization of the FCVI of composite plates.[3,4]

CVI MODEL

The modeling of CVI involves the mathematical description of transport and reaction phenomena within a simulation domain. The simulation domain for the tube FCVI system includes the fibrous preform, fixturing, and open gas space. The open spaces include the gas injection system and the area between the preform and the heating element. Fundamental processes to be modeled include heat transfer by conduction, convection, and radiation, transport and reaction of gaseous reactant species, and pressure-driven flow of the gas. Differential equations representing these phenomena can be written in the following steady-state form:

$$\nabla(\rho \mathrm{u} \phi) = \nabla \cdot (\Gamma \nabla \phi) + S \qquad [1]$$

where ϕ is temperature, pressure, or concentration, u is the gas velocity, ρ and Γ are constants, and S is a source term. Using the finite volume method of Patankar, the discretized version of this equation is solved over the simulation domain which is divided into control volumes.[5]

Heat Transfer

The heat transfer equation contains both diffusion and convection components,

$$\nabla\left(C_p \, u \, T\right) = \nabla \cdot (\mathrm{K} \nabla T) + S \qquad [2]$$

and a source term:

where C_p is the heat capacity of the flowing gas and K is the thermal conductivity of the material. The source term S contains any heat generated or absorbed by the volume element, such as heat from chemical reactions or from absorption of microwave energy. This source term also will be used to account for the thermal radiation.

Calculation of the diffusive and convective contributions to the heat balance for each volume element is straightforward given the flow rate and heat capacity of the gas, the thermal conductivities of the materials, and the thermal boundary conditions. The heat flux terms for each volume element depend only on these quantities and on the temperatures of the adjoining volume elements. Since the radiation contribution may depend on the temperatures of more distant volume elements, these cannot be included as flux terms in the same manner. Instead, these are calculated and included as a source term. To do this a ray tracing program is coupled to the main finite-volume program as a pre-processing step. Based on the discretization of the simulation domain the ray tracing program calculates the view factors of the control volume surfaces. The view factors are then stored for later use. During the solution of the heat transfer equation the view factors are used to calculate the energy exchange between the radiating surfaces by standard formulas based on the nodal temperatures. The radiant energy is then added as a source term to the heat flow equation. To obtain a self-consistent solution several iterations of the heat flow equation are required to incorporate the non-linear behavior of the radiant energy exchange.

Mass Transport and Reaction

The flow of the carrier gas and the concentrations of reacting species are determined by differential equations in the form of equation [1]. For pressure-driven gas flow,

$$\nabla \cdot \left(\frac{k}{\mu V} \nabla P \right) = 0 \qquad [3]$$

where k is the Darcy permeability for the material of each volume element, V is the gas molar volume, and μ is the gas viscosity. This formulation of gas transport does not include source or convective (inertial) terms. It will not be accurate for high velocity gas flow in open reactors but is suitable for the pressure-driven gas flow through semi-permeable materials as is the case for FCVI.

The transport equation for the reacting species includes convection, diffusion, and

$$\nabla(u\ C_i) = \nabla\cdot\left(D_i^{eff}\,\nabla C_i\right)+S \qquad [4]$$

source terms,

where C_i is the species concentration and D_i^{eff} is the effective diffusion coefficient for species i.

Two species are included in the relationship for SiC deposition, methyltrichlorosilane (MTS) and HCl. The MTS is the input species which decomposes into solid SiC which deposits on the preform fibers and gaseous HCl, which is a by-product. The matrix deposition rate depends on the concentrations of both species. The carrier hydrogen, while playing a catalytic role, is not considered.

The coupled systems of differential equations for temperature, pressure, and chemical species concentration are solved in the steady-state. For a selected time increment the local reaction rate is used to calculate a new density for each preform volume element. A new steady-state solution is then calculated and the density incremented again, producing a series of "snap shots" of the densification process.

MODELING TUBULAR GEOMETRY

In a preliminary effort, the CVI model has been applied to a system for preparation of tubular composites by FCVI. The preform is made up of seven layers of

Nextel 312^{TM} (alumino-borosilicate fiber, 3M Company, Minneapolis, MN) cloth. The calculations are performed in cylindrical geometry due to its ease of use and symmetry. The preform, fixturing, and open gas space are discretized into a grid of radial and axial volume elements. No discretization in the θ-direction is considered. The grid size chosen for the modeling domain is 31 radial volume elements by 49 axial volume elements. The preform itself is discretized into six radial volume elements and 29 axial volume elements. The preform is 37 cm in length and 6.4 mm in thickness with an inside diameter of 4.8 cm, and has a 40% fiber volume.

The transport properties for all materials in the modeling domain are defined in separate material files. The thermal conductivities for the graphite, stainless steel, preform, and ceramic fiberboard which make up the structure of the system are functions of temperature. The hydrogen heat capacity, viscosity, and binary diffusivities of MTS and HCl in hydrogen are also functions of temperature. The, thermal conductivity, permeability, and surface area of the preform are functions of fractional density.

Several key boundary conditions are applied to the model. The preform is heated by a cylindrical furnace which surrounds it and is lined with a graphite coating chamber. The thermal gradient is imposed by a stainless steel cooling line that is positioned along the centerline of the system. The temperatures of the graphite coating chamber and stainless steel cooling line are fixed. The total molar flux and mole fraction of MTS are specified at the gas inlet, which is at the centerline on the left side of the preform. Atmospheric pressure is fixed at the gas exhaust and the ends of the domain are specified as adiabatic.

The modeling considered in this paper investigates three key parameters that affect the CVI process: The temperature of the graphite coating chamber; the ratio of hydrogen to MTS (alpha), and the hydrogen flow rate. The temperature range is 1100°C to 1200°C, the alpha range is 5 to 10, and the hydrogen flow rate range is 2.5 to 7.5 l/min.

Figure 1 shows the preform density profile after 24 hours of infiltration at the baseline modeling parameter values of 1200°C, an alpha of 5, and a hydrogen flow rate of 5 l/min. The profile represents a longitudinal section of the tube with the hot side at the

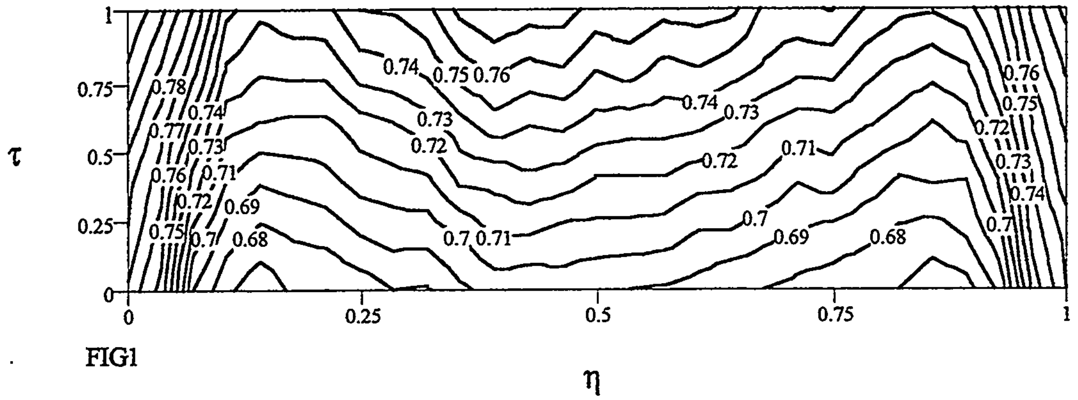

FIG1

Figure 1: Density profile at baseline conditions.

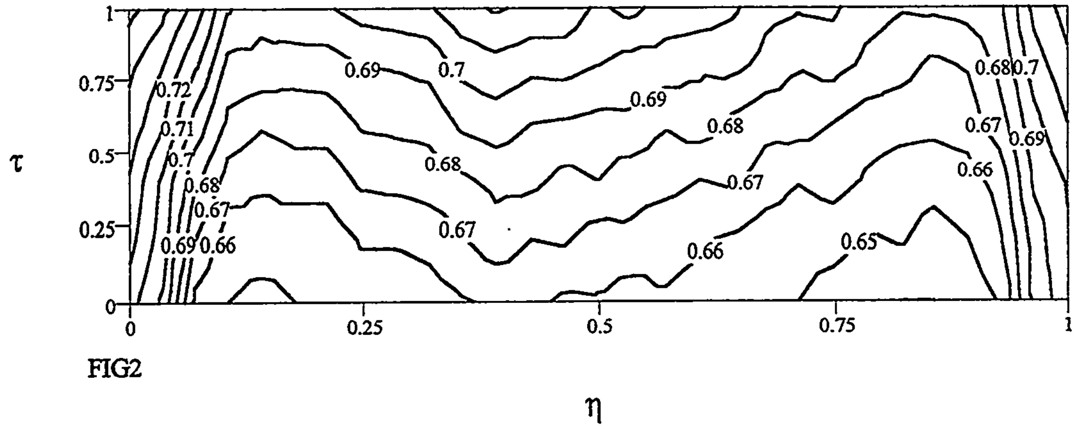

FIG2

Figure 2: Density profile when alpha = 10.

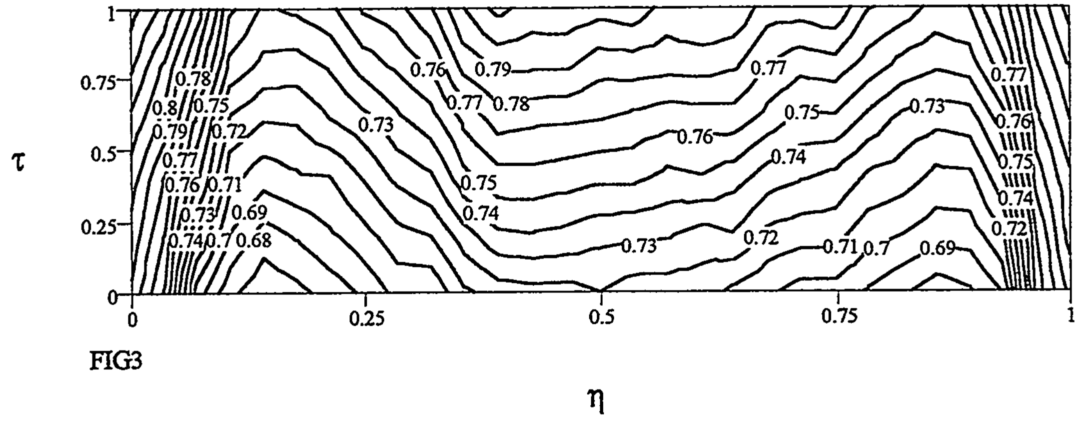

FIG3

Figure 3: Density profile when hydrogen flow rate = 7.5 l/min.

top and the cooled side at the bottom. τ is the dimensionless thickness and η is the dimensionless length. Figure 2 illustrates an increase in alpha to 10 and Fig. 3 uses a hydrogen flow rate of 7.5 l/min. Figures 4 and 5 show preform temperature profiles at the baseline conditions at the start of infiltration and after 12 hours, respectively.

The density profiles in Figs. 1-3 show approximately the same radial and axial gradients. The densities are highest at τ=1 and η=0 and 1. The fractional density is higher in these areas because of the higher temperature. The higher temperature at the ends is due to the graphite felt insulation placed just outside the preform. In Fig. 2, the absolute density values are somewhat lower across the preform. The higher alpha used in Fig. 2 lowers the MTS concentration in the gas phase and thus lowers the SiC deposition rate. Due to the greater reactant flux, the absolute densities in Fig. 3 are slightly higher than those of Fig. 1.

In Fig. 4, the temperature gradient across the preform thickness at η=0.5 is about 80°C. At lower η, near the gas inlet, the gradient is greater due to the radial convective gas cooling. Figure 5 shows the temperature profile after 12 hours of infiltration. The radial temperature gradient is reduced to 50°C due to enhanced radial heat conduction by the SiC matrix in the gas inlet region.

EXPERIMENT

An initial infiltration experiment has been attempted utilizing a tubular preform of the same material and dimensions as that described in the modeling efforts. The Nextel™ preform was rigidized by impregnation with a resin to prevent it from sagging in the horizontal furnace. The infiltration conditions utilized were a hydrogen flow of 5 l/min, an alpha of 4.5, a coating chamber temperature of 1200°C, and a centerline coolant temperature of 50°C. The infiltration time was 24 hours.

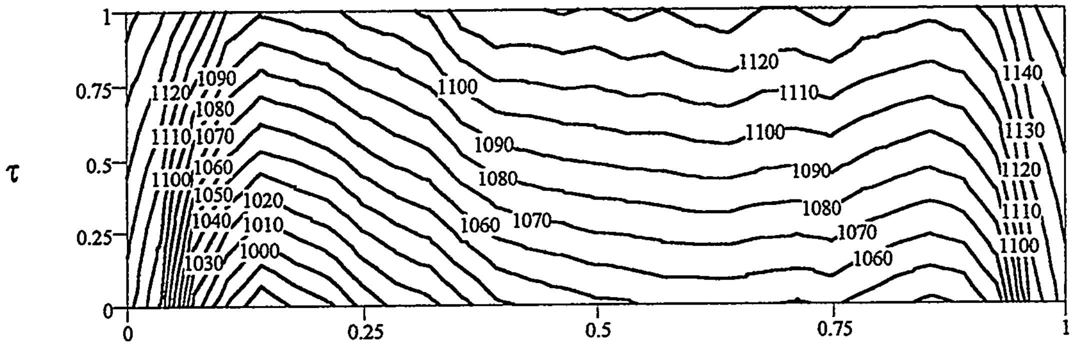

FIG4

Figure 4: Baseline temperature profile at the start of infiltration.

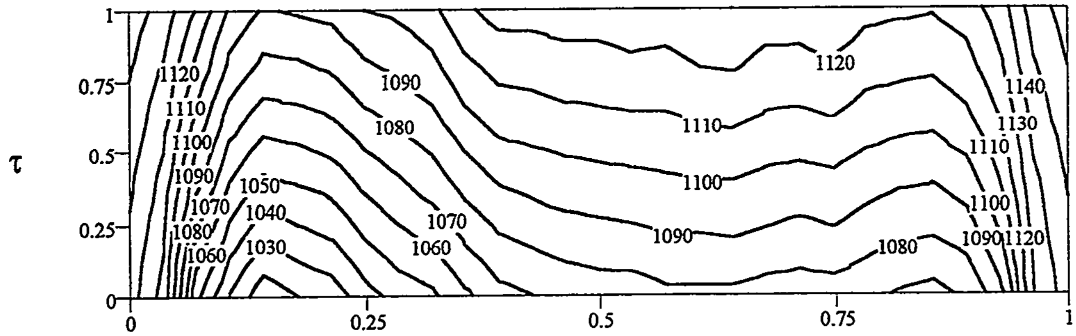

FIG5

Figure 5: Baseline temperature profile after 12 hours of infiltration.

Figure 6: Photograph of Nextel 312TM, SiC matrix composite tube fabricated by FCVI.

Figure 6 is a photograph of the tube showing that, at least superficially, it is well-infiltrated. The average fractional density based on weight is approximately 80%. However, adjustments for the somewhat heavy overcoating of the inner surface of the tube may cause some uncertainty. The model estimated an average preform fractional density of 76% after 24 hours of infiltration.

CONCLUSIONS

The efforts to model the FCVI of tubular geometries has indicated generally successful conditions for infiltration. Decreasing the coating chamber temperature increases the densification time. This reduces the temperature across the preform, causing slower deposition rates. Increasing alpha also increases the densification time. At higher hydrogen flow rates, the densification time decreases. However, a higher gas flow imposes a higher temperature gradient near the gas inlet.

Application of the modeling conditions to experiment gave initial indications that high quality composite tubes can be fabricated, which is also indicated by the experimental results. Future efforts will be focused on better validating the model through comparison with experiment, optimizing processing time and composite density, and increasing the preform outer diameter to 10 cm.

ACKNOWLEDGEMENTS

The comments and suggestions of T. N. Tiegs and L. L. Snead are gratefully acknowledged.

REFERENCES

1. W. J. Lackey and A. J. Caputo, *U. S. Patent No. 4,580,524* (April 8, 1986).

2. T.M. Besmann, B.W. Sheldon, R.A. Lowden, and D.P. Stinton, *Science* **253**, 1104 (1991).

3. T.M. Besmann, in *Proc. High Temperature Matrix Composites II, Ceramic Transactions,* A. G. Evans and R. Naslain, Editors, **58**, p. 1, American Ceramic Society, Westerville, OH (1995).

4. W.M. Matlin, D.P. Stinton, T.M. Besmann, and P.K. Liaw, in Ceramic Matrix *Composites - Advanced High-Temperature Structural Materials*, R.A. Lowden, M.K. Ferber, J.R. Hellman, K.K. Chawla, and S.G. DiPietro, Editors, **365,** p. 309, Materials Research Society, Pittsburgh, PA (1995).

5. S. V. Patankar, *Numerical Heat Transfer and Fluid Flow*, Hemisphere Publishing Corp., New York (1980).

MASS TRANSPORT MEASUREMENTS AND MODELING FOR CHEMICAL VAPOR INFILTRATION

T.L. Starr, D.Y. Chiang, O.G. Fiadzo and N. Hablutzel

School of Materials Science and Engineering
Georgia Institute of Technology
Atlanta, Georgia 30332-0245

ABSTRACT

This project involves experimental and modeling investigation of densification behavior and mass transport in fiber preforms and partially densified composites, and application of these results to chemical vapor infiltration (CVI) process modeling. This supports work on-going at ORNL in process development for fabrication of ceramic matrix composite (CMC) tubes.

Tube-shaped composite preforms are fabricated at ORNL with Nextel™ 312 fiber (3M Corporation, St. Paul, MN) by placing and compressing several layers of braided sleeve on a tubular mandrel. In terms of fiber architecture these preforms are significantly different than those made previously with Nicalon™ fiber (Nippon Carbon Corp., Tokyo, Japan) square weave cloth. We have made microstructure and permeability measurements on several of these preforms and a few partially densified composites so as to better understand their densification behavior during CVI.

INTRODUCTION

The success of forced flow-thermal gradient chemical vapor infiltration (FCVI) for ceramic matrix composites is strongly influenced by the densification behavior and mass transport properties of the preform and partially densified composite. The densification behavior of a particular preform is controlled by the fiber geometry and the weave architecture, and how the residual porosity evolves with increasing density. Gas permeability is a critical factor for FCVI, controlling the movement of reactant within the preform and determining the ultimate density limit for a particular preform in a particular

FCVI reactor. This effort involves experimental measurement of densification behavior and transport properties of CVI preforms. In particular, we have investigated preforms fabricated from Nextel 312 braided sleeve from 3M Company. These results are used in process modeling for optimization of tube fabrication at ORNL. More generally, we are developing models for prediction of these properties and of densification performance.

PREFORM AND COMPOSITE MATERIALS

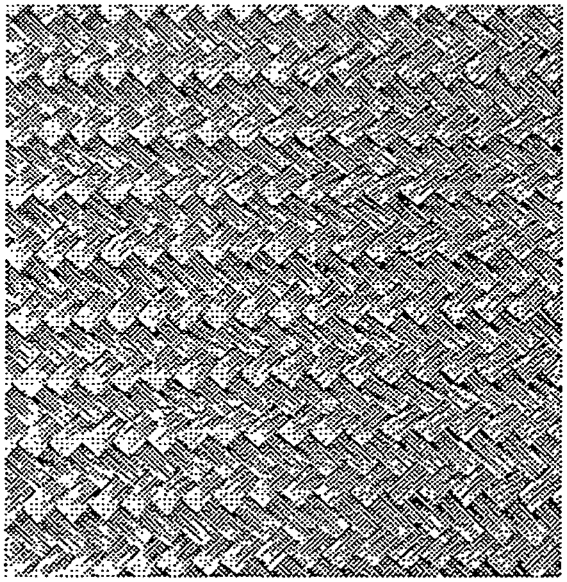

Figure 1. Triaxial braided sleeve is fabricated from Nextel 312 fiber.

Freestanding tube preforms are fabricated from Nextel 312 fiber in the form of triaxial braided sleeve. This material is commercially available and is used for electrical insulation, hose protection, fire zone cable protection and thermocouple insulation, and is available in sizes ranging from approximately 1" to 3" ID. The diameter of the sleeve in somewhat variable and can be adjusted by elongating or compressing the sleeve. The different size sleeves are formed by including different numbers of tows in each yarn and by using different numbers of yarns in the braider. The individual Nextel 312 filaments are oval in shape, have an equivalent diameter of 11 μm and are fabricated in tows of 390 filaments. In the braiding operation 6 to 12 tows are combined and these yarns are placed with a spacing of 8 to 12 picks per inch. Figure 1 shows the structure of this weave for a nominal 2-1/2" ID sleeve. This braid pattern yields closely packed yarns with a crossing pattern of "two-over, two-under" and a crossing angle of approximately 90°. This architecture differs substantially from that of square weave Nicalon fiber cloth which has a "one-over, one-under" crossing pattern and non-close-packed yarns consisting of a single tow of 500 15 μm filaments.

In fabricating the tube preform several of these sleeves are placed over a tubular mandrel, compressed by stretching and stabilized with a thermoset resin. Locally the preform microstructure is a cloth layup with no rotation between adjacent layers. In order to measure the densification behavior and gas permeability of this type of preform, specimens were fabricated by stacking and compressing disks 1.9 cm diameter in an aluminum ring and securing with perforated metal lids. Preform specimens were fabricated with 1", 1-1/2", 2-1/2" and 3" sleeve and with fiber loading of 35 to 40 %v. Composite specimens were extracted from larger disks fabricated at ORNL. These composite all were fabricated with 2-1/2" sleeve, stacked to yield 35, 39 and 43 %v fiber and infiltrated for 5 or 10 hours with conditions of 1200°C furnace temperature, 500 sccm hydrogen and 0.3 g/min MTS. At Georgia Tech we sampled these infiltrated disks by coring out cylindrical specimens 1.4 cm in diameter with a diamond coated core drill. Some of these specimens were mounted for gas permeability measurements while others were mounted and polished for microstructure measurements.

DENSIFICATION BEHAVIOR

Chemical vapor infiltration is, fundamentally, chemical vapor deposition where the deposition surface is, initially, the surface of the reinforcement fibers and, ultimately, the surfaces of the residual pores. Thus, the volume deposition rate consists of two factors: the deposition rate which depends on temperature, pressure and reactant composition and the pore surface area which depends on the fiber architecture and degree of densification of the preform. In developing infiltration conditions for a new type of fiber or preform, one must understand the latter factor.

The surface area function relates the volume of matrix deposited to the deposit thickness. While the initial value of this function can be estimated from fiber size and loading the value after partial densification depends in a complicated way on the architecure. While surface area measurements can be accomplished with high resolution

X-ray tomography[1] or by standard stereology methods[2] we use a method more directly related to the CVI process by measuring the deposit thickness as a function of composite density.

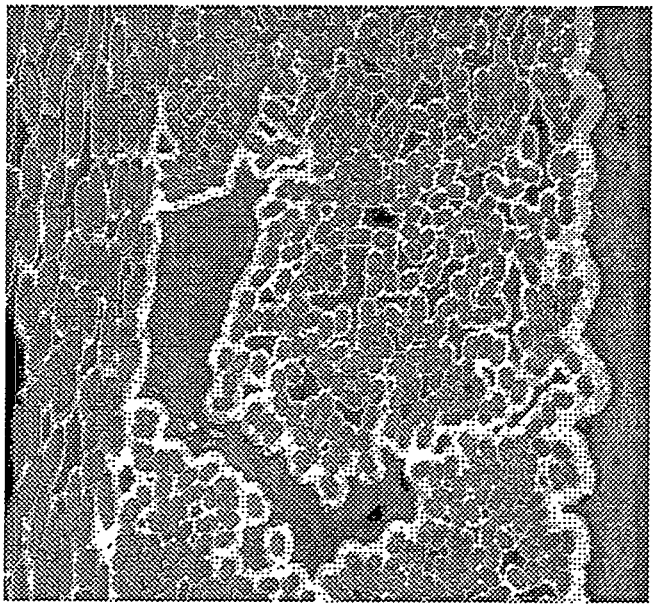

Figure 2. Optical micrograph shows deposition thickness.

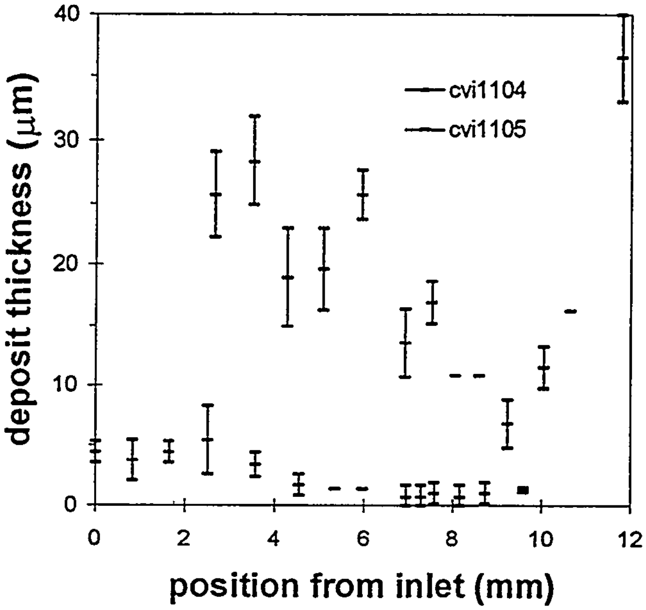

Figure 3. Deposit thickness measurements show significant scatter but average relates to deposition time.

Figure 2 shows the typical microstructure of a partially infiltrated CVI composite. the deposit thickness is measured in the channels between layers where the deposition is not inhibited geometrically by neighboring fibers. Figure 3 shows these measurements for two composite specimens. There is significant scatter among individual values but the overall average for the two infiltration times is clearly different. Figure 4 shows all of these average values plotted versus the density. Density was measured from the mass and geometric volume. The volume fraction solid in the composite calculated from the preform fiber volume fraction plus the volume of matrix deposited assuming silicon carbide at 3.2 g/cm^3. These data include three different packing fractions each at two intermediate densities. The trend is similar to that seen

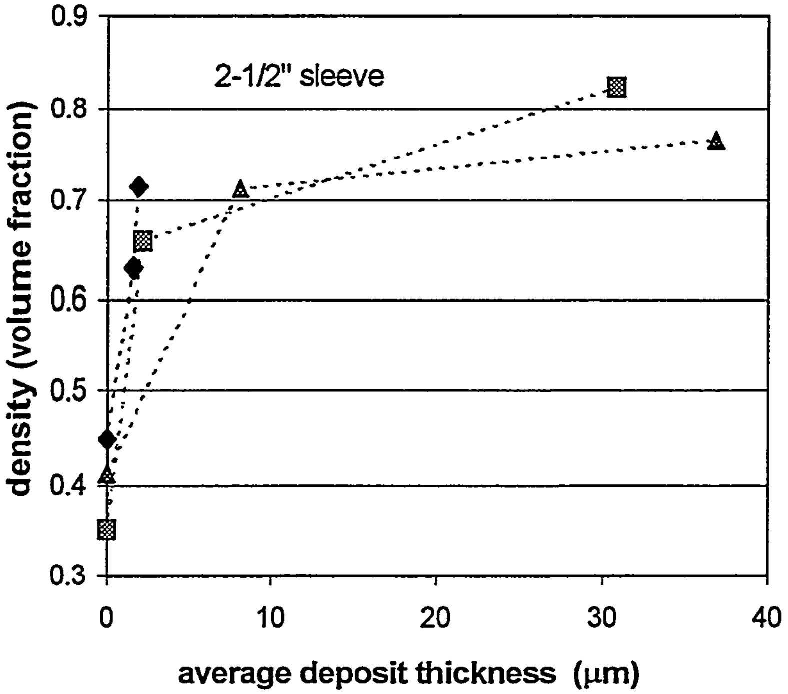

Figure 4. Composite density increases with increasing deposit thickness.

previously with other woven preforms - rapid initial densification as the volume between filaments within the tows is filled, followed by a more gradual densification as the larger spaces between tows (or yarns) is filled.

In order to make these results more useful we fit the data to a semi-empircal interpolation function. The form of this function is based on an understanding of the densification process. There are two scales of porosity: between filaments and between tows. At each scale the initial densification is linear with deposit thickness i.e. the volume deposited is proportional to the thickness deposited. The constant of proportionality is equal to the initial surface area per unit volume S_o. At each scale the deposition rate approaches zero at a maximum value of coating thickness x_c yielding a maximum volume deposited. As a "critical" phenomenon this approach to x_c (the percolation limit) is expected to have an exponential dependence. A functional form that meets these criteria is:

$$V_m = \frac{S_o(1-1/n)x}{\left(1-1/n(x/x_c)^n\right)} \quad for\, x \leq x_c$$

where x is the deposit thickness and n is the exponent controlling the approach to the maximum volume. While there appear to be three parameters in this equation only two are independent due to the requirement that the derivative with respect to x must be zero at x_c. The value of the initial surface area for the tow is calculated from the fiber diameter and packing fraction. Our "fit" to the experiments involves selecting only two values: n (the same for both tow and weave) and the critical thickness for the weave deposit. These are tabulated below and the resulting curve shown in figure 5 where the plot is versus matrix deposited. A better fit could be obtained recognizing that the experimental measurements are for three different initial fiber loadings and different values of S_o and x_c should be specified for each.

The function need for CVI process modeling is the surface area function. This is obtained by differentiating the curve in Figure 5 yielding Figure 6. These results show maximum densification at 40 μm deposition and leaving closed porosity of approximately 20 v%.

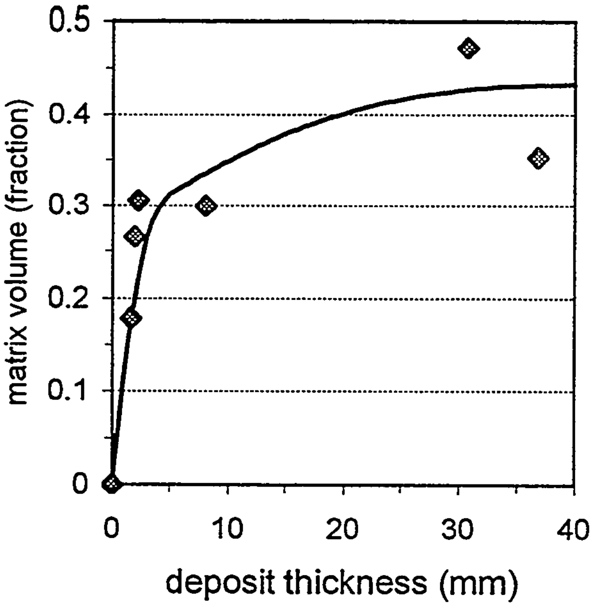

Figure 5. Model compares to experiment with only two empirical parameters.

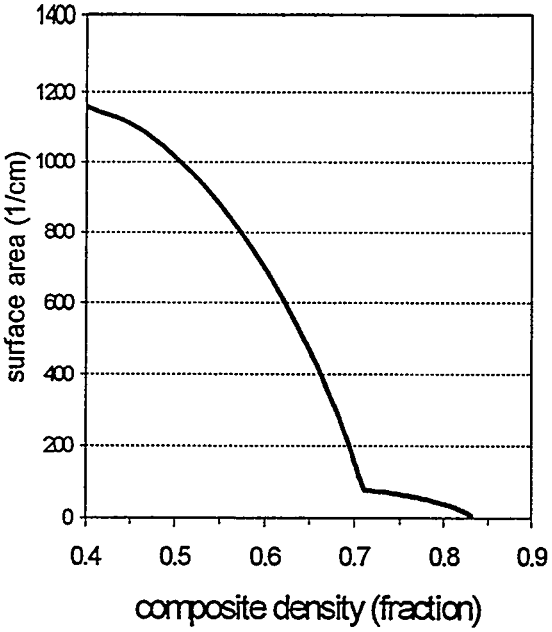

Figure 6. Derivative of densification curve yields surface area function.

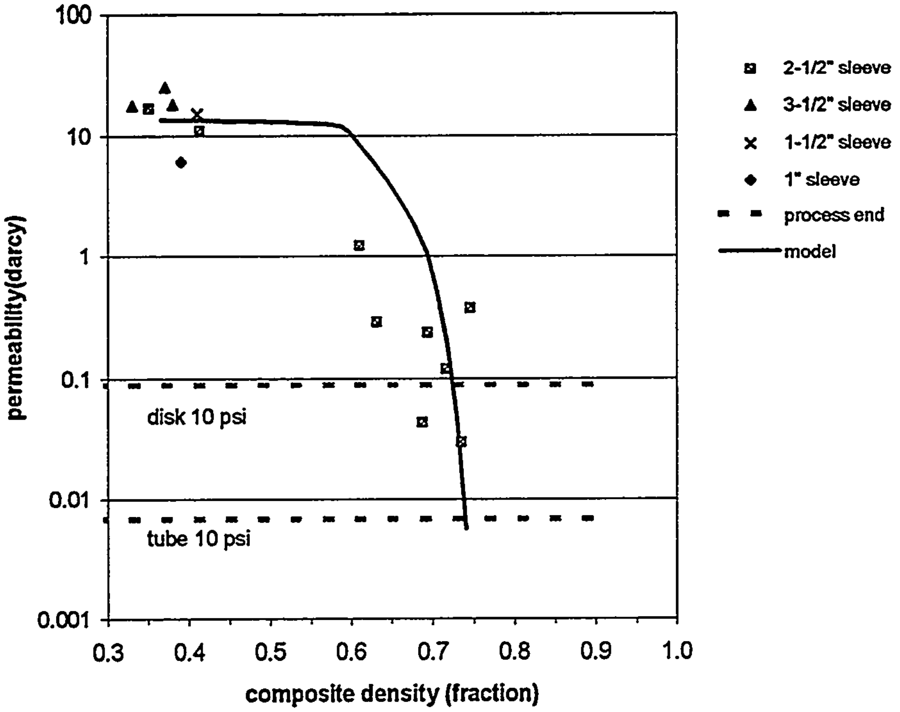

Figure 7. Permeability measurements show more than 20% porosity at end of process.

MASS TRANSPORT MEASUREMENTS

The apparatus and method for measurement of gas permeability has been describe previously[3]. A specimen of preform or porous composite is mounted in an aluminum ring and held in the specimen chamber with o-ring seals top and bottom. The helium gas flow rate is adjusted using a needle valve and the differential pressure across the specimen is recorded for each flow level. The gas permeability is calculated from a linear fit to the flow versus pressure data, the specimen dimensions and the viscosity of helium.

Measurements have been completed for preforms of four different braided sleeve and seven specimens cored from the infiltrated composites. These data are shown in Figure 7. These data are compared to permeability results calculated using a node-bond model[4]. The permeability approaches zero at approximately 80% full density.

DISCUSSION AND CONCLUSIONS

Both the microstructure and the permeability measurements indicate that the maximum density achievable with the braided sleeve preform leaves approximately 20% porosity. This result is in agreement with results for tube infiltration at ORNL reported elsewhere in this proceedings and is in contrast to previous densification with Nicalon square weave cloth preforms which yield densities of up to 95 %. The difference between these is traced to the packing density of yarns within the cloth layers. For the Nicalon cloth yarns are space about 300 μm apart leaving a square through-hole at each yarn crossing point. This hole is wider than the interlayer spacing. Densification can continue until this interlayer channel is filled since the through-holes remain open. For standard Nextel braided sleeve the yarns are tightly packed and the angled through-hole at crossing points is less than 100 μm in diameter, much smaller than the interlayer channel. The maximum density occurs when the through-hole is sealed leaving significant amount of residual porosity between layers.

Other non-standard braid of Nextel are available including a 2" diameter sleeve with 7 picks per inch as shown in Figure 8. This weave provides a significant through-hole in each layer and tube preforms of this braid would be expected to densify to higher density.

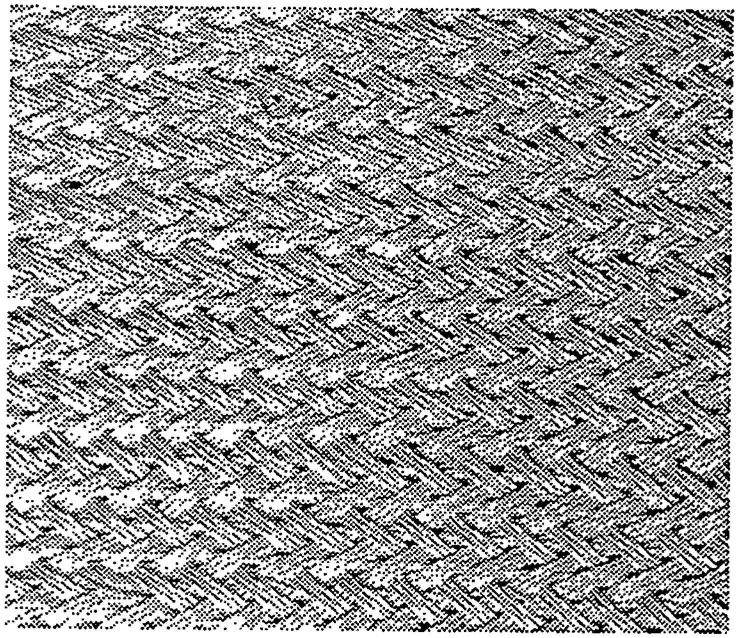

Figure 8. Non-standard braided sleeve (7 picks per inch) should provide better through-cloth transport.

Measurement of densification behavior and gas permeability for the fiber preforms fabricated from braid sleeve provide date for CVI process modeling. These results indicate, however, that a large amount of residual porosity is inevitable for tubes fabricated using the standard sleeve material. Better composite densification should result from using a more open braid pattern.

ACKNOWLEDGEMENTS

We acknowledge the assistance of T.M. Besmann and K.J. Probst at ORNL in providing the partially infiltrated composites and of R.G. Smith of 3M in providing braided sleeve materials.

REFERENCES

1. S-B. Lee, S.R. Stock, M.D. Butts, T.L. Starr, T.M. Breunig and J.H. Kinney, "Pore Geometry in Woven Fiber Structures: 0°/90° Plain-weave Cloth Lay-up Preform," Journal of Materials Research, accepted for publication (1997)
2. E. E. Underwood, Quantitative Stereology, Addison-Wesley, Reading, Mass., 1970
3. T.L. Starr and N. Hablutzel, "Measurement of Gas Transport Through Fiber Preforms and Densified Composites for Chemical Vapor Infiltration," Journal of the American Ceramic Society, accepted for publication (1997)
4. T.L. Starr, "Gas Transport Model for Chemical Vapor Infiltration," Journal of Materials Research 10(9) 1-7 (1995)

OXIDATION-RESISTANT INTERFACE COATINGS FOR NICALON/SiC COMPOSITES

D. P. Stinton, T. M. Besmann, and R. A. Lowden

Oak Ridge National Laboratory
Oak Ridge, Tennessee

P. K. Liaw and S. Shanmugham

University of Tennessee
Knoxville, Tennessee

ABSTRACT

Nicalon/SiC composites with thin C and C/oxide/C interfaces were fabricated. The oxide layers, mullite and Al_2O_3-TiO_2, were deposited by a sol-gel process, while the C layer was deposited by a chemical vapor infiltration method. The fabricated composites were flexure tested in both as-processed and oxidized conditions. Composites with C and C/oxide/C interfaces retained graceful failure even after 500 h oxidation at 1000°C, but with reduced flexural strengths.

INTRODUCTION

It is well established that the fiber-matrix interface plays a key role in determining the mechanical properties of ceramic matrix composites [1-3]. Currently, Nicalon-fiber/SiC-matrix composites owe their good mechanical properties at room temperature to either carbon © or boron nitride (BN) interfaces, which provide a weak interfacial bond. However, C and BN oxidize at elevated temperatures resulting in degradation of mechanical properties of these composites in oxidizing environments [3]. Hence, alternative oxidation-resistant interface materials need to be identified and developed.

Recent analytical and finite element modeling studies have indicated that low modulus interfacial coatings may be desirable to reduce residual radial compressive stresses at fiber-matrix interfaces which develop upon cooling from processing to room temperature [4, 5]. Two oxides, mullite and aluminum titanate, were chosen as interface materials for Nicalon/SiC and Nextel/SiC composites based on their relatively low modulus and their good oxidation resistance at elevated temperatures.

Mullite and aluminum titanate precursor sols were developed for coating applications [6, 7]. High temperature X-ray diffraction studies in air identified that mullite crystallizes at or above

950°C, while aluminum titanate forms at or above 1300°C. Nicalon tows were embrittled during the formation of mullite at 1000°C, and hence, there is a need to protect the fibers by an inert material during the sol-gel oxide processing. The aluminum titanate formation temperature is high and would damage the Nicalon fibers. However, Nicalon fibers dip-coated in an aluminum titanate sol and heat treated at 1000°C for 10 h in air, forming an Al_2O_3-TiO_2 mixture, were not embrittled. Based on the non-embrittlement of the fibers, the Al_2O_3-TiO_2 mixture was chosen as an alternative to aluminum titanate for an interface material. Thermochemical analysis also identified the need to protect the oxide coatings from the HCl attack, a by-product of the SiC matrix deposition reaction. In order to protect the fibers and oxides during processing, a C coating was selected because of its inertness and ease of processing.

To study the effect of protecting the fibers by an inert material during sol-gel oxide coating, oxide/C, and C/oxide/C interfaces were used with Nicalon/SiC composites, and the results were reported earlier [8]. Since composites with C/oxide/C interfaces exhibited higher flexural strengths than composites with oxide/C interfaces in the as-processed condition, C/oxide/C interfaces were given further consideration. On this basis, Nicalon/SiC composites with C/oxide/C interfaces were chosen for further investigation and a control sample, Nicalon/SiC composite with a thin C (40 nm) interface, was also fabricated.

EXPERIMENTAL PROCEDURE

Table 1 summarizes the fabricated Nicalon/SiC composites along with their interfaces, sols used for the deposition of oxides, and the C deposition time. The mullite coating was deposited using either an ethanol or 2-methoxy ethanol based mullite precursor sol, while the Al_2O_3-TiO_2 coating was deposited from an aluminum titanate precursor sol. The C layer was deposited using argon and propylene as reactants for either 15 or 30 min.

Processing of Nicalon/SiC composites involve three steps: preparation of the Nicalon preform, deposition of the interface coatings, and the infiltration of the SiC matrix. The procedure used for fabricating Nicalon/SiC composites is described in detail elsewhere [6, 8], however, a brief description is given below. Fibrous preforms were prepared by stacking 50 layers of Nicalon cloth (45 mm in dia) in a 0°/30°/60° sequence in graphite holders to a thickness of 12.5 mm thick. The C coating was deposited under isothermal and reduced pressure conditions using argon and propylene on the virgin as well as oxide-coated Nicalon preforms. The oxide precursor coatings were produced on C-coated Nicalon preforms by vacuum infiltration of the oxide sol followed by drying at 110°C in air. This process was repeated 3-4 times till a desired coating thickness of 150-300 nm was obtained (determined by weight gain). Then, the oxide precursor coatings obtained on the preforms were heat treated in argon at 1050°C for 1 h to produce the oxide coatings. This was followed by the deposition of the outer C layer. Finally, the SiC matrix was deposited using a forced-flow thermal gradient chemical vapor infiltration process, with methyltrichlorosilane and hydrogen as reactants.

Table 1: Nicalon/SiC composites samples

CVI#	Interface	Sol used for oxide deposition	C deposition time	Oxidation time (h) at 1000°C in air
1077	C	-	30 min	24, 200, and 500
986	C/mullite/C	Ethanol based mullite precursor sol	Inner C: 15 min Outer C: 15 min	24, 200, and 500
1080	C/mullite/C	2-methoxy ethanol based mullite precursor sol	Inner C: 15 min Outer C: 15 min	24, 200, and 500
1002	C/Al_2O_3-TiO_2/C	Aluminum titanate precursor sol	Inner C: 15 min Outer C: 15 min	24, 200, and 500
1066	C/Al_2O_3-TiO_2/C	Aluminum titanate precursor sol	Inner C: 15 min Outer C: 15 min	24, 200, and 500

24 flexure bars of dimensions ~ 2.5 x 3.0 x > 33 mm were obtained from each of the fabricated composites using a standard grinding and cutting procedure. The geometrical density was determined from the weight and dimension measurements of each bar. Four to six specimens were flexure tested at room temperature in the as-processed condition and again after oxidation at 1000°C for 24 h, 200 h, and 500 h. Flexural strengths of composite bars were determined using a four-point bend test fixture (with 20 or 30 mm outer span and 10 mm inner span) on an Applied Testing System machine equipped with a 4375 N load cell. The specimen was placed in the fixture and loaded during the downward motion of the crosshead. The crosshead speed utilized was 2.54 mm/min.

After flexure testing, samples which did not completely fracture were broken by hand for fracture surface examination. The fracture surfaces were examined using a Hitachi S-800 SEM equipped with an energy dispersive X-ray system. The fiber-matrix interfaces of selected samples were examined by transmission electron microscopy using a Hitachi HF-2000 cold field emission gun microscope at 200 kV, which is equipped with a Noran/4 II EDX system. EDS patterns were obtained on fiber-matrix interfaces and were used to identify the coatings.

RESULTS AND DISCUSSION

Table 2 summarizes the geometrical density of fabricated composites along with the inner and outer C layer coating thickness, based on weight gain. The C in the control sample, composite with a C interface, was 43 nm thick. In other composites, the inner C and outer C coatings were each < 30 nm thick. The oxide coating thickness values are not indicated in Table 2 since some of the oxide coatings adhere to the graphite holder, and hence, a good estimate of their thickness cannot be obtained from the weight gain measurements.

Table 2. Density of the fabricated composites along with the C coating thickness (based on weight gain)

CVI #	Density (g/cm^3)	Inner C layer thickness (nm)	Outer C layer thickness (nm)
1077	2.36±0.14	43**	-
986	2.47±0.06	22	21
1080	2.40±0.11	22	21
1002	2.46±0.06	28	27
1066	2.45±0.07	16	16

** control sample where the total C thickness was 43 nm

Table 3 summarizes the flexural strength results of fabricated composites. It should be noted that all the fabricated composites exhibited graceful failure (composite behavior) in both as-processed and oxidized conditions. In the as-processed condition, flexural strengths of composites were between 255 to 311 MPa, and the CVI 1080 composite (C/mullite/C interface) had the highest flexural strength. The control sample, composite with a C interface, had a flexural strength of 311±74 MPa, and is comparable to the value obtained by Walukas [9] for a composite with a 40 nm thick C interface (325±8 MPa). Flexural strengths of the composites decreased with increasing exposure time at 1000°C in air. The CVI 1066 composite (C/Al_2O_3-TiO_2/C interface) and the CVI 1080 composite (C/mullite/C interface) underwent the minimum (21%) and maximum percentage reduction (40%) in flexural strength, respectively, after 500 h oxidation at 1000°C. The composite with a C interface had a 32% strength reduction after 500 h oxidation at 1000°C.

Table 3. Flexural strengths of fabricated composites in the as-processed as well as oxidized conditions

CVI #	Interface	Flexural Strength (MPa) As-processed	Oxidation at 1000°C in air 24 h	200 h	500 h
1077	C	311±74	238±43	224±62	214±68
986	C/mullite/C	268±52	260±61	200±47	184±28
1080	C/mullite/C	320±24	238±54	239±39	193±27
1002	C/Al_2O_3-TiO_2/C	255±35	189±45	217±35	159±20
1066	C/Al_2O_3-TiO_2/C	298±23	314±29	257±64	234±52

In the as-processed condition, the fracture surfaces of composites with C, C/mullite/C, and C/Al_2O_3-TiO_2/C interfaces displayed considerable amount of fiber pullout. However, with increased exposure time at 1000°C, the fracture surfaces revealed reduced fiber pullout, and the fiber pullout was confined to the interior. The samples displayed only brittle fracture along the periphery. An illustration of this effect is shown in Fig. 1.

The persistence of graceful failure in a composite with a C interface even after 500 h oxidation at 1000°C in air, is similar to that reported by Walukas [9]. Walukas [9] observed substantial amount of fiber pullout in the interior in a composite with a thin C interface (40 nm) even after 1000 h oxidation at 1000°C yet with 42% strength reduction, while the regions near the edges were embrittled. His TEM study identified that C was retained in the interior, and hence, the graceful behavior might have been due to the remaining presence of a C interface in the composite.

The TEM study of a CVI 986 composite (C/mullite/C interface) sample in the as-processed condition indicated that the mullite coatings were non-uniform i.e., the mullite layer was absent in many fiber-matrix interfaces. In fiber-matrix interfaces where the C/mullite/C interface was observed, the inner and outer C coatings were each 20 nm thick, while the mullite was ~70 nm thick.

In the CVI 1002 composite, the TEM study identified that the C/Al_2O_3-TiO_2/C interface was present and appeared uniform. The inner and outer C layers were each 30 nm thick, while the Al_2O_3-TiO_2 interface was 30-50 nm thick. Both Al_2O_3 and TiO_2 were crystalline. After oxidation at 1000°C for 500 h in air, the TEM images indicated that the C layers were replaced by SiO_2, but the Al_2O_3-TiO_2 layer was intact. Hence, in the oxidized condition, only a SiO_2/Al_2O_3-TiO_2/SiO_2 interface was observed. Further, the Nicalon fiber surface was oxidized such that 30-50 nm of SiO_2 was observed on the fiber. Thus, the decrease in strength of composite with a C/Al_2O_3-TiO_2/C interface may also be attributed to fiber degradation. Interface C layers may have been retained in the interior of the C/Al_2O_3-TiO_2/C sample after oxidation since it was not clear where the TEM images were obtained. Hence, there is uncertainty involved in the extent to which C is replace by SiO_2.

Nicalon/SiC composites with C, C/mullite/C, and C/Al_2O_3-TiO_2/C interfaces retained damage-tolerant behavior even after 500 h oxidation at 1000°C in air. As examples, Figs. 2 and 3 show the load vs. displacement curves of a CVI 1077 composite (C interface), and a CVI 1066 (C/Al_2O_3-TiO_2/C interface) composite as-processed and after oxidation at 1000°C for up to 500 h in air.

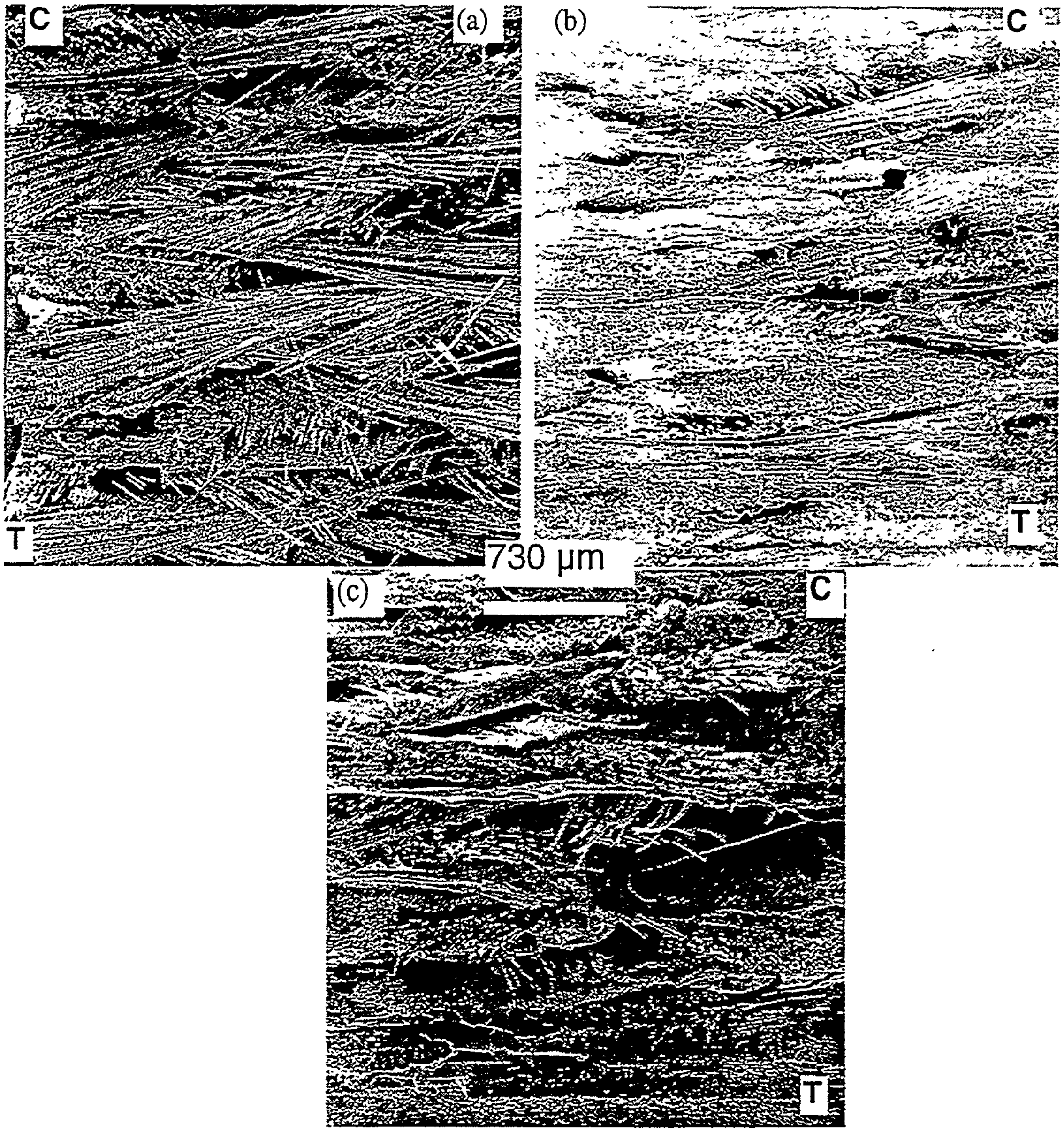

Fig. 1. Fracture surface of a CVI 986 composite sample (a) as-processed condition, (b) after 24 h oxidation at 1000°C, and (c) after 500 h oxidation at 1000°C

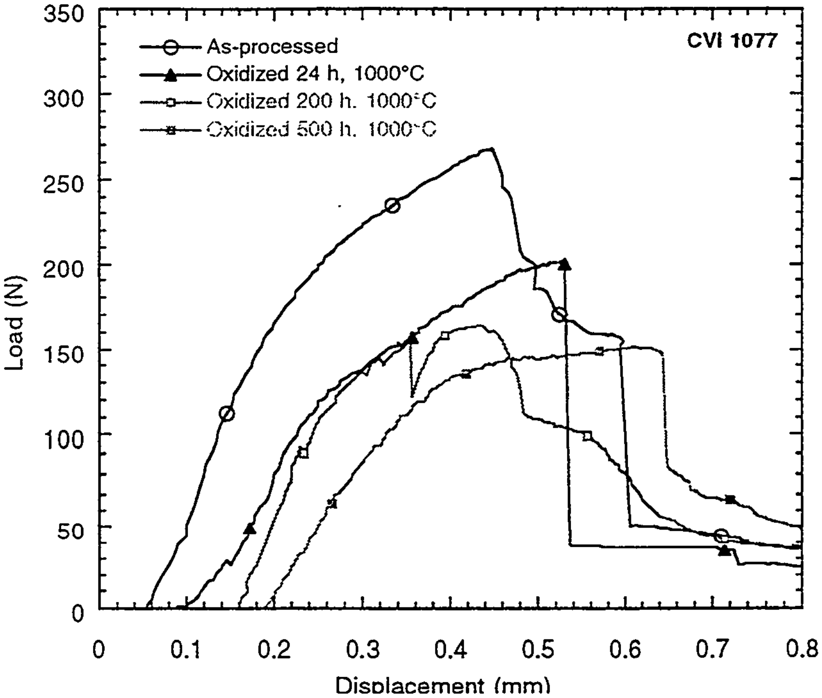

Fig. 2. Representative load vs displacement curves for a CVI 1077 (C interface) composite in the as-processed and oxidized conditions

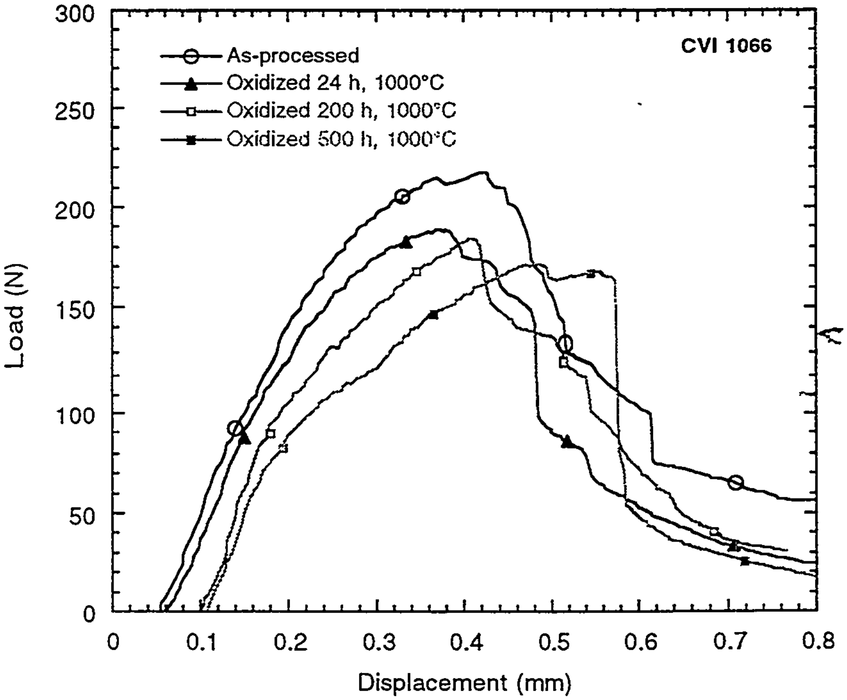

Fig. 3. Load vs displacement curves for a CVI 1066 (C/Al_2O_3-TiO_2-C interface) composite as-processed and after oxidation at 1000°C for up to 500 h in air

CONCLUSIONS

Nicalon/SiC composites with thin C and C/oxide/C interfaces retained damage-tolerant behavior even after 500 h oxidation at 1000°C, but with reduced flexural strengths (21-40%). With increased exposure time at 1000°C, flexural strengths as well as fiber pullout amounts were reduced, and the fiber pullout was confined to the sample interior. TEM analysis indicated that the C layers were replaced by SiO_2, however, there is uncertainty involved in the extent of SiO_2 replacement.

REFERENCES

1. R. J. Kerans, "Issues in the Control of Fiber-Matrix Interface Properties in Ceramic Composites," Scripta Metall. et Mater., 31 [8], 1079-84 (1994).

2. J. J. Brennan, "Interfacial Characteristics of Glass-Ceramic Matrix/SiC Fiber Composites," J. de Physique, Colloque C5 Suppl., 10 [49], 791-809 (1988).

3. R. Naslain, "The Concept of Layered Interphases in SiC/SiC Composites," pp. 23-40 in High Temperature Ceramic Matrix Composites II: Manufacturing and Materials Development in Ceramic Transactions, Vol. 58, Edited by A. G. Evans and R. Naslain, The American Ceramic Society, Ohio, 1995.

4. C. H. Hsueh, P. F. Becher, and P. Angeline, "Effects of Interfacial Films on Thermal Stresses in Whisker-Reinforced Ceramics," J. Am. Ceram. Soc., 71 [11], 929-33 (1988).

5. S. Shanmugham, D. P. Stinton, F. Rebillat, A. Bleier, T. M. Besmann, E. Lara-Curzio, and P. K. Liaw, "Oxidation-Resistant Interfacial Coatings for Continuous Fiber Ceramic Composites," Ceram. Eng. Sci. Proc., 16 [4], 389-99 (1995).

6. S. Shanmugham, P. K. Liaw, D. P. Stinton, T. M. Besmann, K. L. More, W. D. Porter, A. Bleier, and S. T. Misture, "Development of Sol-Gel Derived Coatings for Nicalon/SiC Composites," pp. 71-78 in Advanced Synthesis and Processing of Composites and Advanced Ceramics II, Ceramic Transactions, Vol. 79, The American Ceramic Society, 1996.

7. S. Shanmugham, "Processing and Mechanical Behavior of Nicalon/SiC and Nextel/SiC Composites with Sol-Gel Derived Oxide Interfacial Coatings," Doctoral Dissertation, The University of Tennessee, Knoxville, Tennessee, May 1997.

8. D. P. Stinton, E. R. Kupp, J. W. Hurley, R. A. Lowden, S. Shanmugham, and P. K. Liaw, "Oxidation-Resistant Interface Coatings for SiC/SiC Composites," Fossil Energy Program Annual Progress Report for April 1995 Through March 1996, ORNL-6902, pp. 21-29, June 1996.

9. D. Walukas, "A Study of the Mechanical Properties and Oxidation Resistance of Nicalon/SiC Composites with Sol-Gel Derived Oxide Interfacial Coatings," Masters Thesis, The University of Tennessee, Knoxville, Tennessee, May 1993.

CORROSION PROTECTION OF SIC-BASED CERAMICS WITH CVD MULLITE COATINGS

M.L. Auger and V.K. Sarin

Boston University
Department of Manufacturing Engineering
Boston, MA 02215

For the first time, crystalline mullite coatings have been chemically vapor deposited on SiC substrates to enhance its corrosion and oxidation resistance. Thermodynamic and kinetic considerations have been utilized to produce mullite coatings with a variety of growth rates, compositions, and morphologies. The flexibility of processing can be exploited to produce coated ceramics with properties tailored to specific applications and varied corrosive environments.

INTRODUCTION

Power plants with increased efficiency, fewer emissions, and lower costs has lead to the current development of a new generation of materials. Ceramic coatings are being considered for turbine components such as combustors, blades, stators, seals, and bearings [1]. Under such conditions ceramics are better suited to high temperature environments than metals. Silicon-based ceramics are currently the leading candidate materials for high temperature applications because of their unique combination of high strength and low thermal conductivity, low thermal expansion, good high temperature stability and oxidation resistance. SiC is limited by its susceptibility to specific high temperature corrosive environments. These environments include but are not limited to hot gas streams containing trace amounts and combinations of impurities such as SO_x, NaCl, and O_2 [2]. Combined with the inherent liability of monolithic ceramics to contact stress failure, this corrosion resistance limitation has lead to the development of protective coatings. Innumerable coatings have been developed yet none has met the complex requirements of high temperature engines [3].

Mullite has been targeted as a potential coating material for silicon based ceramics such as SiC. In addition to traditional refractory applications, mullite has received considerable attention as a high temperature material because of its unique ability to retain its strength, resist creep, and avoid thermal shock failure at elevated temperatures [4,5,6,7]. Stoichiometric mullite is quoted as $3Al_2O_3 \bullet 2SiO_2$ yet exists between 57 and 74 mole% Al_2O_3. The crystal structure of mullite is a modified defect structure of sillimanite ($Al_2O_3 \bullet SiO_2$) in which the mullite stoichiometry is achieved by substituting Si^{4+} ions with Al^{3+} ions in the tetrahedral sites and forming an oxygen vacancy [8,9]. The well accepted defect structure is expressed as $Al^{VI}_2(Al^{IV}_{2+2X}Si_{2-2x})O_{10-x}$ where x denotes the amount of missing oxygen and VI and IV denote six-fold and four-fold coordination. Stoichiometric mullite is orthorhombic and theoretically fits between sillimanite (x=0) and alumina (x=1). Solid solubility depends on the formation process and the cooling rate with extreme Al_2O_3 concentrations resulting from temperatures in excess of 2000°C and rapid cooling rates.

Previous attempts to grow mullite coatings by various processing methods have met with limited success [10]. Most commonly reported techniques require a post deposition heat treatment to convert the amorphous alumina-silicate into crystalline mullite [11,12]. Deposition of plasma sprayed mullite coatings was reported; however, inherent porosity in the coatings resulted in the migration of corrodants through the coating after a few hundred hours [13]. To overcome these deficiencies, the direct formation of chemically vapor deposited (CVD) mullite coatings has been investigated. The CVD process results in dense adherent coatings with the ability to control microstructural and morphological properties.

THERMODYNAMIC ANALYSIS

Equilibrium thermodynamics was performed on the $AlCl_3$-$SiCl_4$-CO_2-H_2 system to establish equilibrium reaction products at various operating conditions. This analysis has been detailed in previous publications [14,15]. and were used to create CVD phase diagrams that help establish guidelines for input conditions for producing mullite and other compounds at equilibrium. The overall equilibrium reaction yielding mullite from the reactant gases utilized in the CVD process is theorized to be the following:

$$6AlCl_3 + 2SiCl_4 + 13CO_2 + 13H_2 \rightarrow 3Al_2O_3{\bullet}2SiO_2 + 13CO + 26HCl \quad (1)$$

The results of the previous analysis determined that low concentrations of chlorides need to be used to obtain high deposition efficiency and carbon free deposits.

KINETIC CONSIDERATIONS

A comprehensive thermodynamic analysis is necessary but not sufficient for understanding the CVD process parameters required to grow mullite coatings. Analyzing the kinetic steps, in particular the rate limiting step, involved in the coating deposition is also essential. Current studies focus on collecting experimental data concerning the kinetics of CVD mullite formation using $AlCl_3$, $SiCl_4$, H_2, and CO_2. Kinetic considerations are being taken from the formation of the well established oxide coatings Al_2O_3 and SiO_2 using chloride reactants. The formation of Al_2O_3 proceeds via this hydrolysis reaction:

$$CO_2(g) + H_2(g) \rightarrow CO(g) + H_2O(g) \qquad (2.1)$$

$$2AlCl_3(g) + 3H_2O(g) \rightarrow Al_2O_3(g) + 6HCl(g) \qquad (2.2)$$

It has been shown that the reaction rate of $AlCl_3$ with O_2 is extremely slow while $AlCl_3$ reacts vigorously with H_2O. $AlCl_3$, H_2, and CO_2 exhibit a moderate reaction rate and avoid homogenous nucleation [16]. The reaction proceeds via reaction (2) where reaction (2.1)is labeled the water-gas shift reaction. It has also been stated that SiO_2 is formed via the hydrolysis mechanism at 1000°C, yet it is unclear whether SiO2 can easily form via another mechanism [17]. Experimentally it has been found that the rate is proportional to the concentration of both reactants (assuming the reaction is irreversible). Hence the rate equation for H_2O production is

$$R_{H2O} = k[CO_2]^n[H_2]^m \qquad (3)$$

In this equation, k is called the rate constant for this reaction. It is independent of concentration yet will vary with temperature according to the Arrhenius relation. The factors n and m refer to the rates of the equation and are not necessarily equal to the stoichiometry of the formation equation. For instance if $n = 1$ the reaction is considered first order with respect to carbon dioxide.

The water-gas shift reaction has been extensively studied due to its applicability to metal oxide reactions [18]. Analysis of the reaction over the temperature range 400 to 1050°C suggest separate low temperature and high temperature reaction paths. The low temperature reaction path is dominant at temperatures below 800°C and is extremely sensitive to trace impurities such as oxygen. The high temperature reaction is homogenous and dominant at temperatures in excess of 800°C. The respective low and high temperature mechanisms (determined by measuring CO concentration) are as follows:

$$\text{Low Temperature: } dC_{CO}/dt = 7.6\text{x}10^4\text{Exp}(\frac{-39,200}{RT}*)[H_2]^{1/3}[CO_2] \qquad (4)$$

$$\text{High Temperature: } dC_{CO}/dt = 1.2\text{x}10^{13}\text{Exp}(\frac{-78{,}000}{RT}*)[H_2]^{1/2}[CO_2] \qquad (5)$$

*activation energy is stated in cal/mole

The activation energy of SiO_2 and Al_2O_3 on Si substrates varies according to experimental conditions. Two similar studies performed in cold-walled CVD reactors state an SiO_2 activation energy of 82kcal/mol [19]. and an Al_2O_3 activation energy of 34.8kcal/mol [20]. These separate studies agree with numerous experimental observations in which Al_2O_3 deposition is particularly sensitive to trace impurities in the gas mixture resulting in homogenous (powdery) nucleation [21]. These previous kinetic studies have been used as guides for CVD mullite yet may not be used directly as the kinetics of the mixed chloride reaction will vary from the kinetics of the separate systems.

EXPERIMENTAL METHODS

A CVD reactor consisting of a vertically hot-walled reactor with a resistively heated three-zoned furnace was used for the experiments. Polished bars of 3 x 4 x 20 mm Hexaloy SiC (Carborundum Company, Niagara Falls, NY) were used as substrates. $AlCl_3$ was formed *in situ* by flowing Cl_2 with Ar as a carrier and dilutant through heated Al chips. $SiCl_4$ vapor was introduced by evaporating the liquid at room temperature. CO_2 and H_2 were mixed with the chlorides prior to entering the deposition reactor. Excess H_2 was present to ensure complete reduction of the metal chlorides to form HCl before exiting the reactor. The deposition technique is detailed in previous literature [22]. All depositions were performed at 950°C and a pressure of 75 torr. All coatings were characterized using x-ray diffraction (XRD) and scanning electron microscopy (SEM). Selected coatings were analyzed with electron diffraction, transmission electron microscopy (TEM), and scanning transmission electron microscopy (STEM).

RESULTS AND DISCUSSION

The effect of the input Al:Si ratio on the resultant mullite coating was investigated. The ratio of Al:Si was varied from pure SiO_2 to pure Al_2O_3 with composite coatings varying between 1:1 to 4:1. Experimentally there are numerous methods to achieve the desired input Al:Si molar ratios. The two methods explored in this study are 1) varying the total partial pressure of metallic chlorides (P_{MClx}) by altering the flow rate of $AlCl_3$ and holding the flow rate of $SiCl_4$ constant and 2) holding P_{MClx} constant and varying both $AlCl_3$ and $SiCl_4$ to achieve the desired ratio. The effect of varying the Al:Si ratio through varying P_{MClx} is shown in Figure 1. An initial increase in growth rate is seen as $AlCl_3$ is introduced at an Al:Si ratio of 1:1 and P_{MClx} of 0.33 torr The coatings produced at a 1:1 ratio and P_{MClx} of 0.33 torr were not usually mullite when examined through XRD and exhibited a high degree of non-uniformity. TEM analysis reveled that these coatings were a nano-crystalline mixture of γ-Al_2O_3 and amorphous SiO_2. This nano-crystalline layer was evident in all samples tested at all input ratios. Details of similar structural analysis may be found in a previous study [23]. The growth rate of the coating continues to decrease as the $AlCl_3$ flow rate is increased to an Al:Si ratio of 4:1 and P_{MClx} of 0.93 torr.

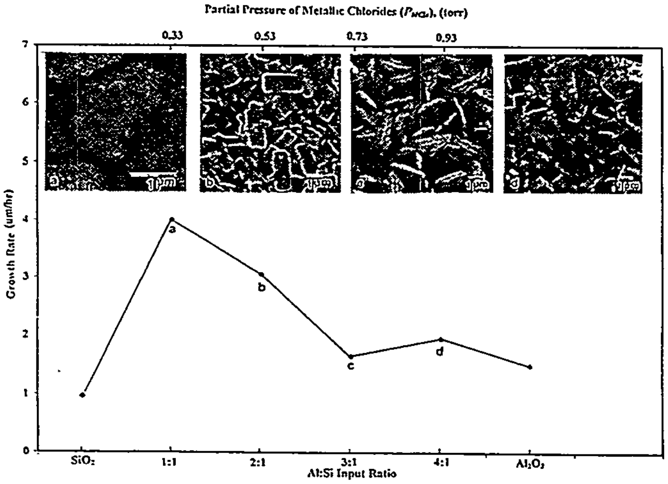

Figure 1: Growth rate of mullite vs. reactant Al:Si ratio and variable metallic chloride partial pressure

The degree of homogenous nucleation (powder formation) and non-uniformity in the coating continued to increase as the Al:Si ratio increased. The surface morphology of the coating becomes more faceted as the input Al:Si ratio increases. Previous studies of CVD mullite coatings have shown that increased Al content increases the faceted nature of the coating [17]. Mullite coatings grown with an input Al:Si ratio of 2:1 were uniform, fine grained, and highly faceted with a growth rate of 3 μm/hr. The growth rate for Al_2O_3 stated in Figure 1 is an average value taken from several literature sources under similar conditions. Attempts to deposit Al_2O_3 using mullite processing conditions resulted in significant homogenous nucleation. Pure SiO_2 coatings under these conditions were found to be amorphous.

The effect of varying the Al:Si ratio by increasing P_{MClx} on the initial nano-crystalline region is shown in Figure 2. The thickness of the nano-crystalline region decreases as the input Al:Si ratio increases. Compositional analysis on the 2:1 and 3:1 samples, carried out in an STEM using a 40nm electron probe, indicate a variation in the Al:Si ratio across the thickness of the coatings. The Al:Si ratio near the substrate is very low, a typical value is 0.326 and is presumed to be SiO_2 at the substrate coating interface. The Al:Si ratio increases as the analysis proceeds through the nano-crystalline region. The coating begins to grow as (001) textured columnar mullite at the point where the Al:Si ratio is between 2.93 and 3.77. This ratio overlaps with the known Al_2O_3 solid solubility of mullite (2.76-3.33). The Al:Si ratio continues to increase through the nano-crystalline region with maximum values approaching 7:1 at the top of the coating. The presence of a nano-crystalline region suggests that mullite is not forming directly as thermodynamics suggests but rather as Al_2O_3 and SiO_2 separately. These molecules are absorbed on the surface of the silicon-based substrate with SiO_2 initially preferred. Mullite nucleates when the Al:Si ratio of the initial nano-crystalline coating reaches a critical value close to that of stoichiometric mullite.

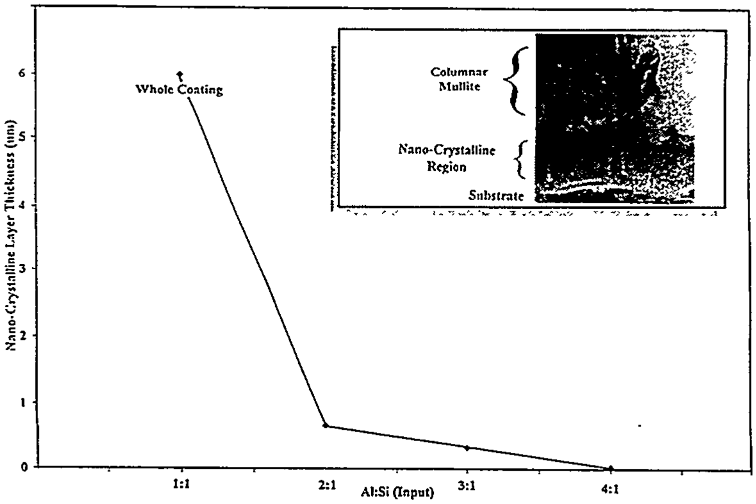

Figure 2: Nano-crystalline layer thickness of mullite coatings vs. reactant Al:Si ratio. Inset is the typical microstructural evolution of mullite coatings on silicon-based materials.

Figure 3 illustrates the effect of growth rate upon the second method of controlling the input Al:Si ratio by maintaining the P_{MCl_x} at 0.53 torr and varying both $AlCl_3$ and $SiCl_4$ to achieve the desired ratio. The constant P_{MCl_x} value was 0.53 torr , the same value for the 2:1 coatings grown in Figure 1. Unlike in the varying P_{MCl_x} matrix the coatings grown at all mixed oxide compositions were uniform, fine-grained, and faceted mullite coatings. The degree of homogenous nucleation did not visually change throughout the mixed oxide range

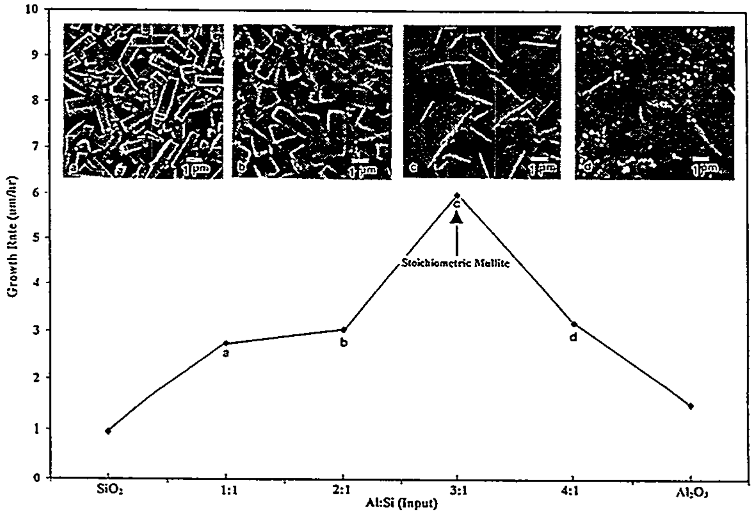

Figure 3: Growth rate of mullite vs. reactant Al:Si ratio at a constant metallic chloride partial pressure (P_{MCl_x}) of 0.53torr

Post-deposition heat treatments were conducted on SiC coated samples with coatings grown by varying P_{MCl_x} to achieve different Al:Si input ratios. Studies were conducted on mullite coatings grown at Al:Si input ratios of 1:1, 2:1, 3:1, and 4:1, as well as SiO_2. Separate coating sets were thermally treated in a vacuum tight chamber at atmospheric pressure in a flowing Ar environment at 1000°C for 100 hours, 1200°C for 100 hours, and 1350°C for 4 hours. The structures of mullite coatings on SiC grown at an input Al:Si ratio of 2:1 and heat treated under these conditions are shown in Figure 4. As the temperature of the annealing treatment increased the surface structure became increasingly featureless. X-ray diffraction of the coatings after heat treatment indicated that the only crystalline phases present were mullite and SiC.

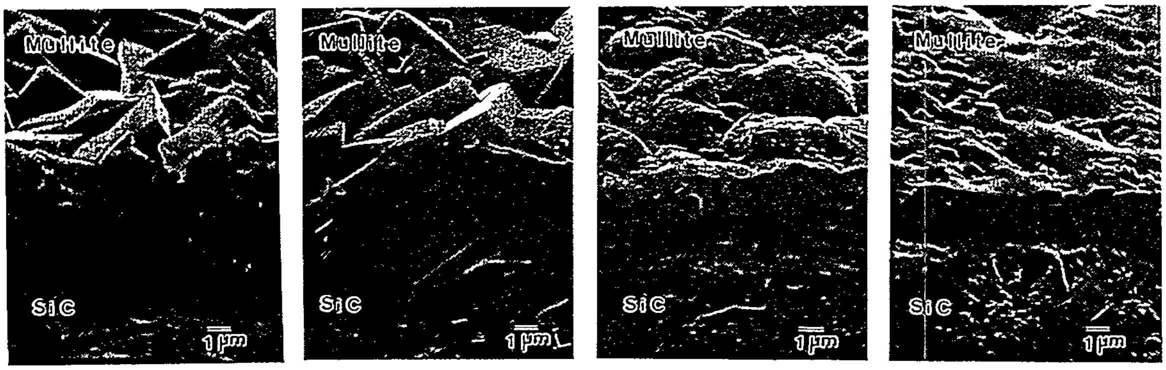

As Grown 1000°C 1200°C 1350°C

Figure 4: Surface structure of mullite a) as deposited, annealed in Ar @ b) 1000°C for 100hr, c) 1200°C for 100hr, c) 1350°C for 4hr

Preliminary experimentation has begun to determine the degree of protection provided by mullite coatings on silicon-based ceramics in corrosive environments. Different corrosive environments may require mullite coatings with slightly different properties. This degree of control may be achieved with CVD mullite coatings. CVD mullite coated SiC was tested in an O_2 rich environment at 1000°C for 100 hours [24]. As shown in Figure 5 an extremely low weight gain is observed past 30 hours of exposure. The extremely low weight change (little formation of oxide) is shown as the weight change versus square root of time(assuming parabolic oxide growth kinetics) for times greater than 30 hours. At this point, there is no statistical difference in the growth kinetics between mullite coated with an input Al:Si ratio of 2:1 (P_{MCl_x} = 0.53 torr), 3:1 (P_{MCl_x} of 0.53 torr), and the slow diffusion rate of O_2 through the protective SiO_2 layer that forms on SiC.

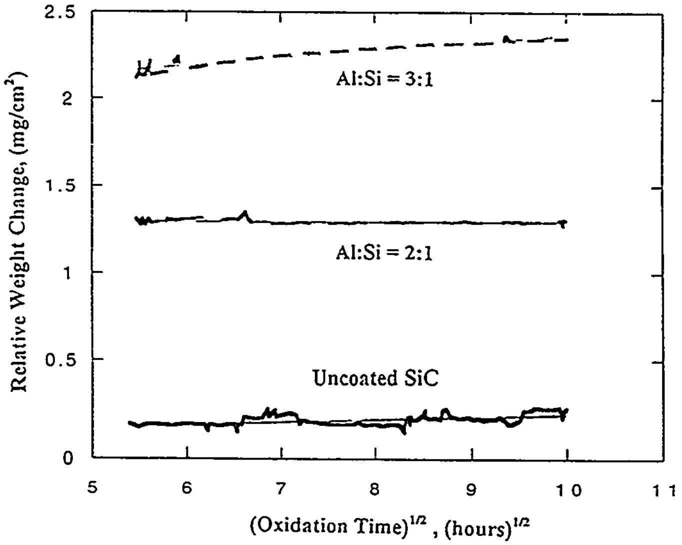

Figure 5: Relative weight change of uncoated SiC and mullite coatings grown at reactant Al:Si ratios of 2:1 and 3:1 on SiC vs. (oxidation time)1/2 in a flowing air environment at 1000°C. [Tortorelli Ref. 24]

CVD mullite coated Si_3N_4 was subjected to a corrosive environment containing Na_2SO_4 and O_2 at 1000°C for 100 hours [25]. The specimens were typically loaded with about 5 mg/cm^2 of Na_2SO_4 and exposed to a flowing oxygen environment in a quartz tube heated to 1000°C. The use of an oxygen environment results in a basic molten salt (i.e., high Na_2O activity), thus facilitating the corrosive reaction of Na_2O with native SiO_2.

The results of uncoated Si_3N_4 and mullite coated Si_3N_4 after exposure are shown in Figure 6. The presence of a Na-containing glassy phase is observed to a depth of ≈ 20 μm below the initial substrate surface in the uncoated sample. Yttrium (used as a sintering aid in Si_3N_4) migrated through the grain boundaries of the substrate to the substrate surface, resulting in the formation of a yttrium depleted zone of ≈ 10 μm. The mullite coated sample was relatively unaffected by the corrosive environment. It was found from TEM study that the remainder of the coating as well as the underlying Si_3N_4 substrate were not affected either microstructurally or compositionally by the corrosion exposure.

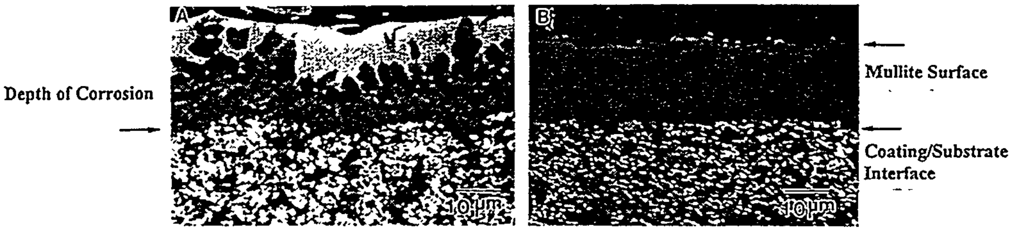

Figure 6: Comparison between a) uncoated Si3N4 and b) mullite coated Si3N4 subjected to a Na2SO4-O2 environment at 1000°C. White areas on surface are corrosion. [W.Lee Ref. 25]

With the desire to tailor CVD mullite coatings on ceramic heat exchangers in coal-fired systems for power production, CVD mullite coated SiC samples were exposed to corrosive coal slag at 1260°C for 300 hours [26]. Corrosive coal slag will form extreme porosity and dramatic pit formation in unprotected SiC. After 300 hours of exposure all mullite coatings (Al:Si input ratios 2:1, 3:1, 4:1 achieved through varying P_{MCl_x}.) exhibited excellent protection. Generally, mullite grown with a lower input Al:Si ratio exhibited a more corrosion resistant surface as shown in Table I. This trend agrees with the as deposited SEM analysis of mullite coatings in which an input Al:Si ratio of 2:1 (P_{MCl_x} 0.53 torr) produced a more uniform coating than an input Al:Si ratio of 4:1 (P_{MCl_x}. 0.93 torr).

Al:Si (Input Ratio)	Observations
2:1	Very Clean, no pitting
3:1	Clean, possible beginning of pit formation
4:1	Clean, possible beginning of pit formation
Uncoated SiC	Corrosion beginning

Table I: Observations of mullite grown with different input Al:Si ratios on SiC and exposed to Baldwin coal slag for 300 hr at 1260°C. [Breder Ref. 26]

CONCLUSIONS

Through the use of thermodynamic and kinetic analysis crystalline mullite coatings have been deposited via chemical vapor deposition upon silicon based materials such as SiC. Altering process parameters such as deposition temperature and reactant partial pressure has resulted in mullite coatings with varied physical and chemical properties such as crystal structure, surface morphology, and chemical composition. Preliminary results have indicated that mullite coatings form an effective barrier to corrosion in high temperature corrosive environments including Na_2SO_4-O_2, oxidation, and coal slag.

ACKNOWLEDGMENTS

Research sponsored by the U.S. Department of Energy, Assistant Secretary for Energy Efficiency and Renewable Energy, Office of Transportation Technologies, as part of the Ceramic Technology Project of the Propulsion System Materials Program, and Fossil Energy AR&TD Materials Program under contract numbers DE-AC05-840R21400 and SC-19X-SS110C with Martin Marietta Energy Systems, Inc. The authors would like to acknowledge Dr. Woo Lee, Dr. Kristen Breder, and Dr. Peter Tortorelli for corrosion testing, Ping Hou for TEM analysis, and Dr. S. Basu for invaluable discussions.

REFERENCES

---

1. W.J. Lackey, D.P. Stinton, et.al., *Advanced Ceram. Mat.*, **2** [1], 24-30, (1987)
2. N.S. Jacobson, *J.Am. Ceram. Soc.*, **76** [1], 3-28, (1993)

3. W.J. Lackey, D.P. Stinton, et.al., ORNL/TM-8959 (1984)
4. I.A. Aksay, D.M.Dabbs, M. Sarikaya, *J. Am. Ceram. Soc.*, **74** [10] 2343-58(1991)
5. P.F.Becher, *J. Am. Ceram. Soc.*, **74** [2] 255-69 (1991)
6. S.Somiya, Y. Hirata, *Am. Ceram. Soc. Bull.*, **70** [10] 1624-32 (1991)
7. R.D. Nixon, S. Chevacharoenkul, R.F. Davis, and T.N. Tiegs, pp. 579-603 in Ceramic Transactions, Vol. 6, *Mullite and Mullite Matrix Composites*, Edited by S. Somiya, R.F. Davis, and J.A. Pask, American Ceramic Society, Westerville, OH, 1990
8. D.G.W. Smith and J.D.C. McConnel, *Mineral. Mag.*, **35** [274] 810-14 (1966)
9. T. Epicier, *J. Am. Ceram. Soc.*, **74** [10] 2359-66 (1991)
10. J. Schienle, and J. Smyth, Final Report, ORNL/Sub/84-47992/1 (1987)
11. K. Okada, N. Otsuka, pp.425-34 in Ceramic Transactions, Vol. 6, *Mullite and Mullite Matrix Composites*, Edited by S. Somiya, R.F. Davis, and J.A. Pask, American Ceramic Society, Westerville, OH, 1990
12. O.R. Monteiro, Zhi Wang, Ian G. Brown, *J. Mat. Res.*, To be Published
13. K.N. Lee, N.S. Jacobson, R.A. Miller, *MRS Bulletin* **19** [10], 35-38, (1994)
14. R.P. Mulpuri, and V.K. Sarin, 19th Annual Cocoa Beach Conference and Exposition on Engineering Ceramics, Cocoa Beach, FL, The American Ceramic Society, Westerville, OH, (Jan. 1995)
15. R.P. Mulpuri, and V.K. Sarin, *J. Mater. Res.*, 11 (6), 1315-24, (1996)
16. Ph, Wong, M. Robinson, *J.Am Ceram. Soc.*, **53**, 617-21, (1970)
17. W.Steinmaier, J.Bloem, *J. Electro. Soc.*,**111** (2), 206-209, (1964)
18. G.L. Tingey, *J. Phy. Chem.*, **70** (5), 1406-1412, (1966)
19. W.Steinmaier, J.Bloem, *J. Electro. Soc.*,**111** (2), 206-209, (1964)
20. S.W. Choi, C. Kim, et.al., pp.233-41 in the proceedings of the IX International Conference on CVD (CVD-IX) , ed. McD. Robinson, The Electrochemical Society Inc., Pennington, NJ, 1984
21. H. Altena, K. Stjernberg, B. Lux, pp. 381-90 in the proceedings of the V European Conference on CVD (Euro-CVD-V), ed. J. -O. Carlsson, Uppsala University, Department of Chemistry, Uppsala, Sweden
22. V.K. Sarin and R.P. Mulpuri, *U.S. Pat. Pending*
23. D.Doppalaupudi, et.al., pp. 664-70 in the proceedings of the XIII Annual CVD Conference, ed. T.M.Besmann, The Electrochem. Soc. Inc. Pennington, NJ, 1996
24. Testing performed by Dr. Tortorelli of ORNL, Oak Ridge, TN
25. W.Y. Lee, K.L. More,Y.W. Bae, *J. Am. Ceram. Soc.*, **79** (9), 2489, (1996)
26 Testing performed by Dr. Breder of ORNL Oak Ridge, TN

THERMAL CYCLING CHARACTERISTICS OF PLASMA SYNTHESIZED MULLITE FILMS

O.R. Monteiro, P.Y. Hou and I.G. Brown

Lawrence Berkeley National Laboratory, University of California, Berkeley, CA 94720

ABSTRACT

We have developed a plasma-based technique for the synthesis of mullite and mullite-like films on silicon carbide substrate material. The method, which we refer to as MePIIID (for Metal Plasma Immersion Ion Implantation and Deposition), uses two vacuum arc plasma sources and simultaneous pulse biasing of the substrate in a low pressure oxygen atmosphere. The Al:Si ratio can be controlled via the separate plasma guns, and the film adhesion, structure and morphology can be controlled via the ion energy which in turn is controlled by the pulse bias voltage. The films are amorphous as-deposited, and crystalline mullite is formed by subsequent annealing at 1000° C for 2 hours in air. Adhesion between the aluminum-silicon oxide film and the substrate increases after this first annealing. We've tested the behavior of the films when subjected to repetitive thermal cycling between room temperature and 1100°C, and found that the films retain their adhesion and quality. Here we review the plasma synthesis technique and the characteristics of the mullite films prepared in this way, and summarize the status of the thermal cycling experiments.

INTRODUCTION

Thin films have been formed by a wide variety of plasma methods[1]. We have developed a plasma-based thin film deposition technique that has the important feature that the ion energy can be controlled widely. Highly adherent, fully-dense films of metals, alloys (including non-equilibrium alloys) and other conducting materials, and their oxides and nitrides, can be formed. In the early stages of the process the ion energy is held in the keV range so as to produce atomic mixing at the film-substrate interface, and in the latter stages of deposition the energy is reduced so as to optimize the film structure and morphology.

We've drawn upon previously existing technology to form a new plasma technique that is a hybrid of several more commonly know methods, including filtered cathodic arc deposition[2,3], ion beam assisted deposition (IBAD)[4-7], ion beam mixing[4-6,8], and plasma immersion ion implantation (piii)[9,10]. In our method, which we've dubbed Mepiiid (*Me*tal *p*lasma *i*mmersion *i*on *i*mplantation and *d*eposition), the object to be implanted is immersed in a plasma of the desired species, formed by a vacuum arc plasma gun and repetitively pulse-biased to a negative voltage[11-15]. A high voltage sheath rapidly forms at the substrate-plasma boundary, and plasma ions are accelerated through the sheath and into the substrate, thereby accomplishing implantation into the substrate of plasma ions at an energy determined by the bias voltage. Because of the surface retention of condensed metal plasma, the process in a metal plasma is quite different from in a gaseous plasma. Ions that are deposited during the pulse-off part of the cycle are deposited on the surface as a monolayer or sub-monolayer film, and ions that are accelerated from the plasma and bombarded into the substrate during the high voltage bias part of the cycle suffer collisions with previously-deposited neutral metal atoms and thus also produce recoil implantation. By varying the proportions of the direct and recoil implantation parts of the cycle (ie, the duty cycle of the pulse biasing) one can tailor the shape of the implantation depth profile, and the range can be tailored by the amplitude of the applied pulse voltage. The whole operation can be time-varied throughout the processing duration, starting for example with a high energy phase so as to create a deep buried layer of the implanted species an ion mixing phase) and slowly changing to a low energy phase whereby a surface film is built up by plasma deposition (an ion beam assisted deposition phase). By controlling the plasma ion energy we thus acquire control over two very important features to the deposition process: the interface width can be tailored, and the film morphology and structure can be controlled. In this way one can synthesize a surface metallic film of precisely controllable thickness having a well-determined and controllable atomically mixed interface with the substrate, and the parameters of the film and the interface can be tailored over a wide range. For purely metallic films, the process is carried out at a vacuum in the 10^{-6} Torr range; oxides and nitrides can be formed by doing the deposition at the appropriate background pressure of oxygen or nitrogen, typically a few tens of microns

In our plasma materials synthesis research program we have shown that highly adherent, high quality films of many different kinds of materials can be formed in this way, including films of metals[16-18], metal oxides[19,20] and oxide ceramics[21-24], optoelectronic materials[25], high-Tc superconductors[26,27], diamond-like carbon[28-30], and multilayer structures with complex layer structures[31-33]. Concise reviews have been presented of the method and applications[34,35].

Of relevance to the present work, we have previously formed alumina films[21,24] and mullite films[22,23], and some observations of the behavior of these films in a high temperature environment and their value as high temperature oxidation resistant coatings have been made. Near-stoichiometric alumina films of thickness ~0.2 - 1 µ on substrates of FeAl (containing ~0.1% Zr) were prepared; the films were amorphous prior to heat treatment and showed an α-alumina phase after heat treating at 1000°C for up to 16 hours. The film substrate adhesion was typically greater than ~70 Mpa (the limit of our measurement) prior to heating, and the adhesion was maintained after repetitive cycling in temperature between ambient and 1000°C. Also, mullite ($3Al_2O_3.2SiO_2$) films have been formed on SiC substrates by mixing together separately produced plasmas of aluminum and silicon. The Al to Si ratio was controlled by the plasma gun parameters and the plasmas blended together in a magnetic multipole plasma homogenizer device. Deposition was done onto appropriately positioned SiC substrates.

Here we report on our evaluation of the performance of plasma-synthesized mullite films on SiC subject to repetitively cycled high temperature excursions. In the following we firstly summarize the plasma synthesis technique as applied for the present purpose, and outline the characteristics of the mullite films formed, followed by a description of the testing processes and the experimental results obtained.

OUTLINE OF THE PLASMA SYNTHESIS TECHNIQUE

Our approach is to immerse the substrate in the dense metal plasma formed by one or more vacuum arc plasma guns while controlling the energy of the depositing ions by the application of a high frequency, repetitively pulsed bias voltage to the substrate during the plasma deposition. Oxygen is added at a suitable low pressure and is incorporated in the growing film primarily by surface oxidation and subsequent recoil implantation. Ion energy is controlled as a function of time, and the film-substrate interface can be tailored and the film structure optimized by the ion beam assist that is inherent to the process.

The vacuum arc is a high current discharge between two electrodes in vacuum in which metal plasma is produced in abundance[2,36-38]. We have made several different embodiments of vacuum arc plasma guns. Here we used a small, repetitively pulsed version operated at a pulse length of 5 ms and repetition rate 1 Hz with arc current typically 300 A. Along with the metal plasma that is generated, a flux of macroscopic droplets (resolidified cathode debris) of size in the range 0.1 - 10 microns is also produced[36-40]. In general it is desirable to remove the solid particulate contamination and this can be done by using a curved magnetic duct (bent solenoid of magnetic field strength a few hundred gauss) which stops line-of-sight transmission of macroparticles while allowing the transport of plasma[41-43]. The overall plasma formation system thus consists of the repetitively pulsed plasma gun in conjunction with a 90° magnetic filter.

Metal oxides can be formed by carrying out the deposition not in a high vacuum environment but in a somewhat higher pressure ambient of oxygen gas; we have found empirically that a pressure in the range 1 - 100 mTorr is suitable for most purposes. In the present work the oxygen background pressure was 5 to 25 mTorr. The oxygen is both entrained in the plasma stream, ionized, and deposited in the plasma state, as well as reacting at the freshly-deposited metallic surface to form aluminum oxide or silicon dioxide. In either case, for the optimal oxygen pressure a near-stoichiometric film of the metal oxide is formed.

Ion energy of the depositing plasma flux is controlled by repetitively pulse biasing the substrate. The pulse duration is ~10 μs and the duty cycle ~10–50%. Pulsing the bias is necessary (for all but the lowest bias voltages) because a high-voltage dc bias would cause a discharge between the substrate and the vessel or the plasma gun; the plasma would be grossly perturbed (because the plasma sheath would expand from the substrate to large distances). The solution is to switch off the bias before a discharge can occur (to limit the sheath expansion to modest distances), let the plasma recover, and then repeat the process; ie, to do the biasing in a repetitively pulsed mode. For the early stages of the deposition the pulse bias is held at a relatively high voltage of -2.2 kV. The mean aluminum ion energy is then 3.75 keV, because the mean ion charge state of the aluminum plasma is 1.7 and $E_i = QV$; for silicon the mean charge state is 1.4 and the mean ion energy 3.1 keV; (the charge state spectra of vacuum arc produced plasmas have been discussed in detail in refs. 44,45). At this energy ions are implanted into the substrate to a depth of up to ~100 Å. The film thus grows on the SiC substrate from a highly mixed interface. When a film thickness of just a few tens of angstroms has accumulated, the pulse bias voltage is reduced, since intermixing with the substrate is no longer a factor and the higher ion energy would sputter away the already-deposited film. Moreover, it is known from a large body of work on ion assisted deposition that a modest ion energy can be highly advantageous for controlling characteristics such as the density, morphology and structure of the film. For the bulk of the plasma deposition process the pulse amplitude is kept at -200 volts.

To deposit films containing several different metallic elements we have combined the operation of two plasma sources, with their magnetic ducts, so that the plasma streams of different elements are mixed together before reaching the substrate. Optionally, a short magnetic multipole "plasma homogenizer" structure can be used also, to better blend the two plasmas and to produce a more uniform plasma density profile; we have incorporated this feature in some of our work [46]. A schematic diagram of the dual-plasma deposition apparatus is shown in Figure 1. The deposition can be carried out synchronously or asynchronously, i.e. the plasma sources can be operated simultaneously or sequentially. Depending on the deposition rate, asynchronous operation may lead to stratification of the film in layers, whereas synchronized operation results in a greater degree of mixing. In the films described here the latter operating mode was chosen so as to maximize the intermixing of the atoms in the solid phase.

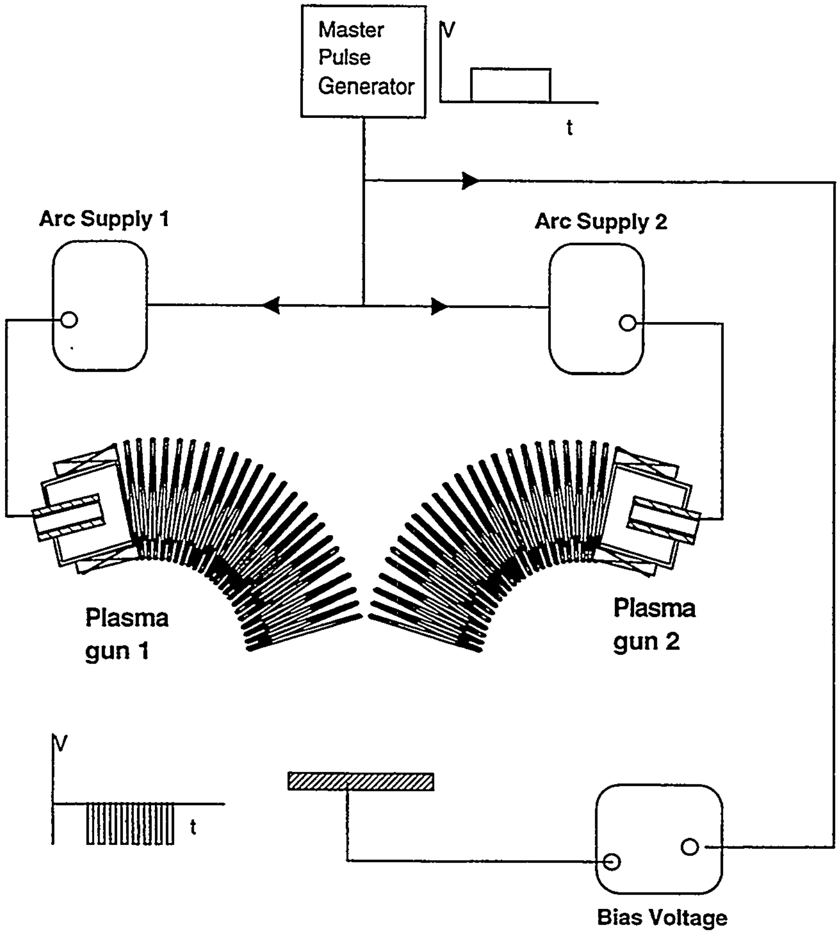

Figure 1 Simplified schematic of the plasma configuration used to form the films.

CHARACTERISTICS OF THE SYNTHESIZED FILMS

Films of silicon-aluminum oxide were synthesized on polished SiC substrates. An edge-on SEM photograph of a typical film is shown in Figure 2. The details of our Mepiiid technique as applied for this specific application have been described elsewhere[22,23]. The films are typically of thickness in the range 0.2 - 2 microns. X-ray diffraction analysis has shown that the as-deposited films are amorphous, with no evidence of crystalline structure or phase separation. Annealing of the films at 1100°C in air for 2 hours results primarily in the formation of crystalline mullite, $3Al_2O_3.2SiO_2$.

Adhesion of the films to the substrate has been investigated using a Sebastian-type pull-tester having an instrumental limit of measurement of about ~70 MPa. We have found that adhesion strength of the as-deposited films is generally in the range 10 - 40 MPa, and the post-annealing adhesion strength is equal to or greater than the instrumental limit of ~70 MPa – i.e., the annealed samples when subjected to a normal pull-test of epoxied studs show failure at the epoxy-film interface and not the film-substrate interface.

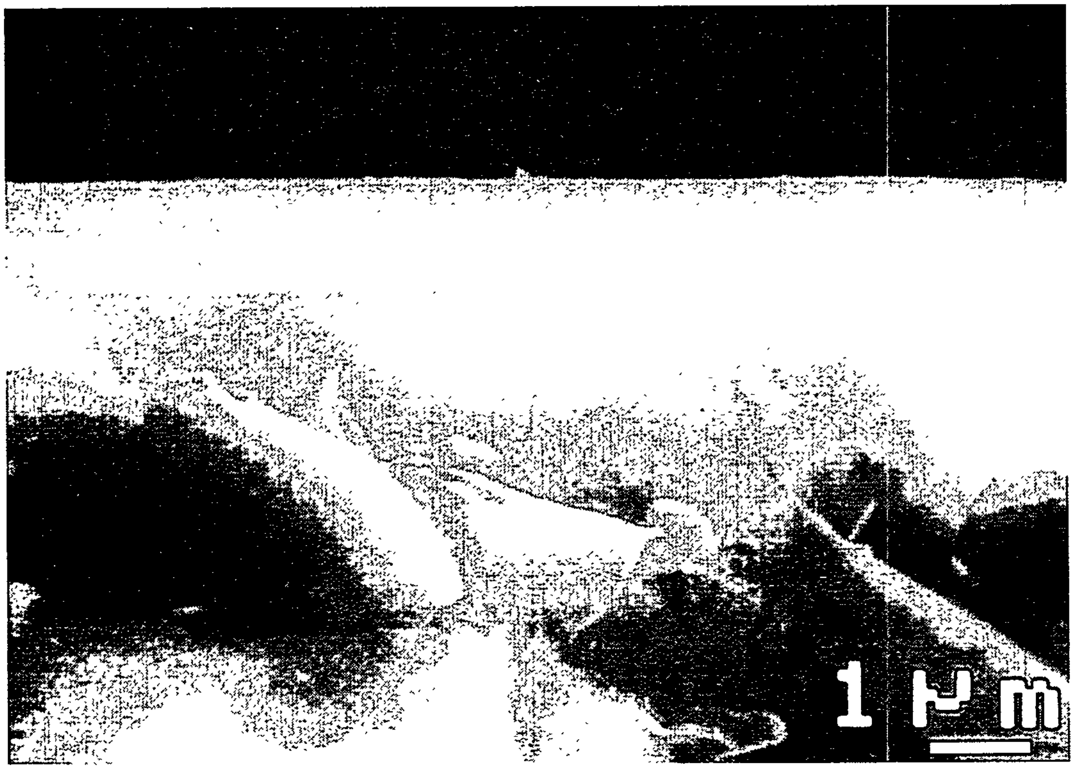

Figure 2. Edge-on scanning electron microscope photograph of a thin film of mullite formed by the dual-source MePIIID process on a silicon carbide substrate. Aluminum and silicon plasmas were combined in the appropriate proportions in a low pressure background of oxygen to form the $3Al_2O_3.2SiO_2$ mullite structure. The film is somewhat over 1 micron in thickness, and is fully dense, non-columnar, highly adherent, smooth, and exceptionally resistant to repeated thermal cycling between room temperature and 1100°C.

THERMAL CYCLING CHARACTERISTICS

We have investigated the adhesion of the mullite films to silicon carbide when subjected to thermal cycling. Each cycle consisted of heating the samples to 1100°C at a rate of 9°C/min, maintaining the substrate at 1100°C for 18 h in air, and cooling it down at a rate of approximately 4°C/min. For the first 5 cycles, adhesion was measured after each heat cycle, and after that adhesion was measured after the 15th and 20th cycle.

In order to characterize the adhesion after thermal cycling we used our Sebastian pull tester. However, in our early work[22,23] we showed that the stress required to debond the mullite film from the SiC substrate often exceeds the maximum strength of the epoxy used (this is the limit of measurement of this technique). Therefore these measurements can provide only a lower limit for the adhesion strength. This has prompted us to use an additional method for characterizing the strength of the bonding between film and substrate.

The method used here for characterizing the interface toughness is based on the indentation method developed by Evans and co-workers[47-49]. This technique involves making micro-indentations in the surface of the oxide film. The indentation creates a plastically deformed zone immediately beneath the surface. Residual stresses developed in the plastic zone provide the driving force for lateral and radial crack growth[50]. If the interface toughness is lower than the toughness of both the film and the substrate, lateral cracks will develop and propagate along the interface, as indicated in Figure 3. Evans and co-workers[47-49] have developed fracture mechanics solutions that allow interfacial fracture energies to be calculated from the size of these cracks. In order for the model to be realistic, the depth of the indent should be less than the film thickness.

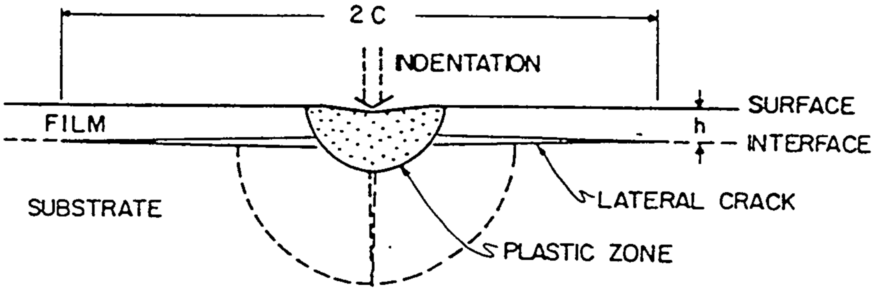

Figure 3: Schematic of an indentation made on a film-substrate sample, showing the lateral crack propagating preferentially along the interface.

Due to the small thickness of the mullite films produced here, the indents did perforate through the film, and therefore our estimates of the interface strength should not be taken too quantitatively. One can make arguments that would imply that perforation of the layer would lead either to an underestimate or to an overestimate of the toughness. Figure 4 is an optical micrograph of an indentation mark, with the lateral crack visible. According to the model presented in Figure 3, this determines the end of the delaminated region. We used a load of 1 kg with a Vickers indenter. In spite of these limitations, the test can still be used comparatively, to show trends. The results of both kinds of tests are shown in Table 1 for the thermal cycling tested. The result of the indentation tests in this Table are shown in terms of the radius of the debonded region observed. A value of zero indicates that no crack was observed upon application of the load. Appearance of lateral cracks after cycling the temperature 15 times suggests some weakening of the interface, though still below the detection limit of the Sebastian pull-test. We plan to extend the thermal cycling to see if the adhesion further deteriorates.

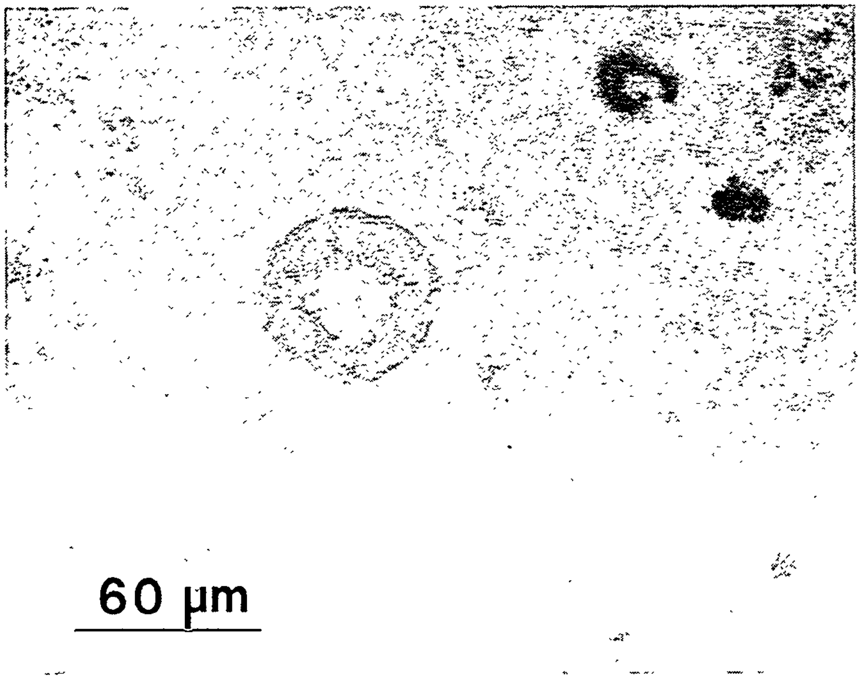

Figure 4: Optical micrograph of a Vickers indent on a mullite film on a SiC substrate. Indentation load was 1000 g.

To illustrate the order of magnitude of the interface strengths determined by the indentation method, we carried out an analysis according to ref. 47 using the model for lateral crack expansion. The following parameters were used for this calculation: crack radius 30 µm, contact load 1000 g, film thickness 0.2 µm, film hardness 30 GPa. The calculated interfacial fracture resistance was then $K_{IC,interface} = 0.8$ MPa $m^{1/2}$. Despite the uncertainties in this value, it compares highly favorably with the fracture toughness for SiC ($K_{IC,SiC} = 4.6$ MPa $m^{1/2}$) and mullite[51] ($K_{IC,mullite} = 2$ MPa $m^{1/2}$).

Cycle No.	Sebastian Pull Test (MPa)	Indentation Test lateral crack size
1	> 70	0
2	> 70	0
3	> 70	0
4	> 70	0
5	> 70	0
10	> 70	0
15	> 70	30 μm
20	> 70	30 μm

Table 1: Film-substrate adhesion strength as determined by a Sebastian-type pull-test, and lateral crack size as determined by a microindentation test, as a function of number of 24-hour thermal cycles between room temperature and 1100 °C.

CONCLUSION

We have successfully deposited mullite films on silicon carbide by combining plasma streams of Al and Si ions produced by vacuum arc plasma guns in a background atmosphere of oxygen. The films are of the stoichiometric $3Al_2O_3.2SiO_2$ composition and fully dense, non-columnar, and smooth. Application of high negative bias voltage to the substrate (ie, high ion energy) is essential for good adhesion between the film and substrate. The adhesion of the as-deposited mullite is high, increases upon annealing of the film, and remains high over subsequent thermal cycling at 1100°C.

Evaluation of sample properties following thermal cycling through a yet greater number of heat cycles is presently under way. Future studies will include: extension of the number of thermal cycles that the coated samples experience in order to determine whether any degradation takes place; detailed microstructural characterization of the mullite-SiC interface; and more accurate determination of interface strength.

ACKNOWLEDGMENTS

We are indebted to Bob MacGill and Mike Dickinson for their support of the LBNL experimental equipment. This work was supported by the U.S. DOE, Office of Advanced Research, Fossil Energy, under Contract Number DE-AC03-76SF00098.

REFERENCES

1. See, for example, the Proceedings of the annual International Conferencer on Metallurgical Coatings and Thin Films (ICMCTF), published as special issues of *Thin Solid Films* and *Surface and Coatings Technology*.
2. R.L. Boxman, P. Martin and D. Sanders (eds), *Vacuum Arc Science and Technology*, Noyes, New York, 1995.
3. D. M. Sanders, J. Vac. Sci. Tech. A7, 2339 (1989).
4. See, for instance, Ion Implantation and Plasma Assisted Processes, edited by R.F. Hochman, H. Solnick-Legg and K.O. Legg, (ASM, Ohio, 1988).
5. *Plasma Processing and Synthesis of Materials*, edited by D. Apelian and J. Szekely, Mat. Res. Soc. Symp. Proc. Vol 98, (MRS, Pittsburgh, 1987).
6. See, for instance, the proceedings of conferences such as those on Ion Implantation Technology, and Ion Beam Modification of Materials, in Nucl. Intrum. Methods, Part B.
7. M. Iwaki, Critical Rev. in Solid State and Mat. Sci. 15 (1989) 473.
8. G.K. Wolf and W. Ensinger, Nucl. Instr. and Meth. B59/60, 173 (1991).
9. J.R. Conrad, J.L. Radtke, R.A. Dodd, F.J. Worzala and N.C. Tran, J. Appl. Phys. 62, 4591 (1987).
10. See the proceedings of the First and Second International Workshops on Plasma-Based Ion Implantation, J. Vac. Sci. Tech. B12, 815-998 (1994), and Surface and Coatings Technol. 85, 1-124 (1996), resp.
11. I.G. Brown. X. Godechot and K.M. Yu, Appl. Phys. Lett. 58, 1392 (1991).
12. I.G. Brown, A. Anders, S. Anders, M.R. Dickinson, I.C. Ivanov, M.A. MacGill, X. Yao and K.M. Yu, Nucl. Instrum. Meth. Phys. Res. B80/81, 1281 (1993).
13. I.G. Brown, in *Plasma Synthesis and Processing of Materials*, edited by K. Upadhya (pub. TMS, Warrendale, PA, 1993).
14. A. Anders, S. Anders, I.G. Brown and I.C. Ivanov, Mat. Res. Soc. Symp. Proc. 316, 833 (1994).
15. A. Anders, S. Anders, I.G. Brown, M.R. Dickinson and R.A. MacGill, J. Vac. Sci. Tech. B12, 815 (1994).
16. S. Anders, A. Anders, I. Brown, F. Kong and F. McLarnon, Surface and Coatings Technol. 85, 75-79 (1996).
17. I. Brown, A. Anders, S. Anders, M.R. Dickinson and R.A. MacGill, J. Vac. Sci. Tech. B12, 823 (1994).
18. M.A. Otooni, I.G. Brown, S. Anders and Z. Wang, Mat. Res. Soc. Symp. Proc. 396, 649 (1996).
19. R.A. MacGill, S. Anders, A. Anders, R.A. Castro, M.R. Dickinson, K.M. Yu and I.G. Brown, Surface and Coatings Technol. 78, 168 (1996).
20. S. Anders, A. Anders, M. Rubin, Z. Wang, S. Raoux, F. Kong and I.G. Brown, Surface and Coatings Technol. 76-77, 167 (19950.
21. I.G. Brown and Z. Wang, 9th Annual Conference on Fossil Energy Materials, Oak Ridge, TN, May 16-18, 1995, Proceedings of conference (U.S. Dept. of Energy, Conf-9505204, ORNL/FMP-95/1), p. 239.
22. O.R. Monteiro, Z. Wang, K.-M. Yu, P.Y. Hou, I.G. Brown, B.H. Rabin and G.F. Kessinger Proc. 10th Annual Conference on Fossil Energy Materials, Knoxville, TN May 14-16, 1996, (Pub. Conf-9605167, ORNL/FMP-96/1, published by US DOE). p. 97.
23. O.R. Monteiro, Z. Wang and I.G. Brown, J. Mat. Res., to be published (1997).
24. P.Y. Hou, K.B. Alexander, Z. Wang and I.G. Brown, in *Elevated Temperature Coatings: Science and Technology II*, edited by N.B. Dahotre and J.M. Hampikian (pub. The Minerals, Metals and Materials Society, 1996); p. 187.
25. S. Raoux, I. Brown, S. Anders, K.M. Yu and I.C. Ivanov, Mat. Res. Soc. Symp. Proc. 392, 241 (1995).
26. M.S. Chae, M.T. Simnad, M.B. Maple, S. Anders, A. Anders and I.G. Brown, Physica C 270, 173-179 (1996).
27. M. S. Chae, M. B. Maple, M. T. Simnad, S. Anders, A. Anders and I. G. Brown, IEEE Trans. Appl. Supercon. 5, 2011 (1995).
28. O.R. Monteiro, I.G. Brown, R. Sooryakumar and M. Chirita, Mat. Res. Soc. Symp. Proc. 444, 93-98 (1997).
29. G.M. Pharr, D.L. Callahan, S,D. McAdams, T.Y. Tsui, S. Anders, A. Anders, J.W. Ager III, I.G. Brown, C.S. Bhatia, S.R.P. Silva and J. Robertson, Appl. Phys. Letters 68, 779 (1996).

30. S. Anders, A. Anders, I.G. Brown, B. Wei, K. Komvopoulos, J.W. Ager III and K.M. Yu, Surface and Coatings Technol. 68/69 388 (1994).
31. O.R. Monteiro, M.-P. Delplancke-Ogletree, J.W. Ager and I.G. Brown, Mat. Res. Soc. Symp. Proc. 438, 599-604 (1997).
32. M.-P. Delplancke-Ogletree, O.R. Monteiro and I.G. Brown, Mat. Res. Soc. Symp. Proc. 438, 639-644 (1997).
33. S. Anders, D.L. Callahan, G.M. Pharr,.T.Y. Tsui and C.S. Bhatia, J. Mat. Res., to be published.
34. I.G. Brown, A. Anders, S. Anders, M.R. Dickinson, R.A. MacGill, O.R. Monteiro, E.M. Oks, S. Raoux, Z. Wang and G. Yushkov, Mat. Res. Soc. Symp. Proc. 396, 467-477 (1996).
35. J.V. Mantese, I.G. Brown, N.W. Cheung and G.A. Collins, in: "Plasma Processing of Advanced Materials", MRS Bulletin 21(8), 52-56 (1996).
36. J.M. Lafferty (ed.), *Vacuum Arcs - Theory and Application*, Wiley, New York, 1980.
37. For a most impressive and comprehensive bibliography of the vacuum arc literature see H.C. Miller, *A Bibliography and Author Index for Electrical Discharges in Vacuum (1897 - 1986)*, pub. by the General Electric Co., document No. GEPP-TIS-366e (UC-13), March 1988; also published in part in IEEE Trans. Elec. Insul. 25(5),765 (1990) and 26(5), 949 (1991).
38. See the Special Issues on Vacuum Discharge Plasmas in IEEE Trans. Plasma Sci. These issues contain selected papers from the biennial International Symposium on Discharges and Electrical Insulation in Vacuum, usually in the October issues in odd-numbered years.
39. D.T. Tuma, C.L. Chen and D.K. Davies, J. Appl. Phys. 49, 3821 (1978).
40. J.E. Daalder, Physica 104C, 91 (1981).
41. I.I. Aksenov, A.N. Belokhvostikov, V.G. Padalka, N.S. Repalov and V.M. Khoroshikh, Plasma Physics and Controlled Fusion 28, 761 (1986).
42. A. Anders, S. Anders and I.G. Brown, Plasma Sources Sci. & Technol. 4, 1 (1995).
43. S. Anders, A. Anders and I.G. Brown, J. Appl. Phys. 75, 4895 (1994).
44. I.G. Brown and X. Godechot, IEEE Trans. Plasma Sci. PS-19, 713 (1991).
45. I.G. Brown, Rev. Sci. Instrum. 10, 3061 (1994).
46. S. Anders, S. Raoux, K. Krishnan, R.A. MacGill and I.G. Brown, J. Appl. Phys. 79, 6785 (1996).
47. S.S. Chiang, D.B. Marshall and A. G. Evans in "Surfaces and Interfaces in Ceramic and Ceramic-Metal Systems" (Eds J. Pask and A.G. Evans), Plenum Press, New York, 1981, p. 603.
48. D.B. Marshall, B.R. Lawn and A.G. Evans, J. Am. Ceram. Soc. 65, 561 (1982).
49. D.B. Evans and A.G. Evans, J. Appl. Phys. 24, 209 (1984).
50. P.Y. Hou and A. Atkinson, Mater. at High Temp. 12, 119 (1994).
51. R. Torrecillas, G. Fantozzi, S. de Aza and J.S. Moya, Acta Mater. 45, 897 (1997).

INFLUENCE OF WATER VAPOR AND SLAG ENVIRONMENTS ON CORROSION AND MECHANICAL PROPERTIES OF CERAMIC MATERIALS*

by

K. Natesan and M. Thiele
Energy Technology Division
Argonne National Laboratory
Argonne, IL 60439

ABSTRACT

Conceptual designs of advanced combustion systems that utilize coal as a feedstock require high-temperature furnaces and heat transfer surfaces that can operate at temperatures much higher than those prevalent in current coal-fired power plants. The combination of elevated temperatures and hostile combustion environments requires the development and application of advanced ceramic materials in these designs. The objectives of the present program are to evaluate the corrosion behavior of candidate ceramic and metallic materials in air and slag environments and evaluate the residual mechanical properties of the materials after corrosion. The program emphasizes temperatures in the range of 1000-1400°C for ceramic materials and 600-1000°C for metallic alloys. Coal/ash chemistries based on thermodynamic/kinetic calculations and slags from actual combustors are used in the program. The materials being evaluated include monolithic silicon carbide from several sources, silicon carbide in a silicon matrix, silicon carbide in alumina composites, silicon carbide fibers in a silicon carbide-matrix composite, and some advanced nickel-base alloys. This paper presents results from an ongoing study of the corrosion performance of candidate ceramic materials exposed to dry air, air with water vapor, and slag environments and the effects of these environments on the flexural strength and energy absorbed during fracture of these materials.

INTRODUCTION

Coal is a complex and relatively dirty fuel that contains varying amounts of sulfur and a substantial fraction of noncombustible mineral constituents, commonly called ash. Conceptual designs of high-performance power systems (HIPPS) that utilize coal as a feedstock require high-temperature furnaces and heat transfer surfaces capable of operating at higher temperatures than those used in conventional coal-fired power plants. The combination of elevated temperatures and hostile combustion environments requires the use of ceramic materials in at least the first few passes of the heat exchangers in these designs.

In addition to conventional steam turbines, HIPPS would employ a combined cycle that uses a gas turbine driven by a working fluid (air) that is separately heated in a high-temperature advanced furnace.[1] The ultimate goal is to produce electricity from coal with an overall thermal efficiency of 47% or greater (compared with ≈35% for current systems) and to reduce CO_2 emissions by 25-30%. The pulverized-coal high-temperature advanced furnace (HITAF) in the HIPPS concept will heat air to an intermediate temperature of ≈1000°C and burn supplemental clean fuel to boost the temperature of air to a turbine inlet temperature of ≥1300°C. Use of supplemental fuel can be reduced as the HITAF technology evolves to permit the heating of air to higher temperatures in the furnace. The HITAF represents a major departure from conventional pulverized-coal-fired boilers in which only steam is raised to a maximum of 530-620°C. The purpose of the HITAF is to heat the clean working fluid, air, to the required turbine inlet temperatures. At the elevated temperatures of the HITAF, transfer of heat from the combustion gases to the working fluid will be dominated by radiative heat transfer, and the design of the heat transfer surface will be critical for the success of the system. Several concepts are under development for the design of the heat transfer surfaces in the HITAF system.[2]

For any of the concepts to be viable for a commercial-scale HIPPS, the heat transfer surfaces must be exposed to much higher temperatures than are prevalent in conventional coal-fired steam-turbine systems. For temperatures of 1000-1300°C, conventional metallic materials do not possess adequate strength properties and/or corrosion resistance for long-term service. In addition, an important difference between the conventional boiler system and the HIPPS is seen in the chemical and physical characteristics of the ash layers that can deposit on the heat transfer surfaces. The deposits are likely to be dominated by alkali sulfates and coal slags in HIPPS rather than by pyrosulfates or alkali-iron-trisulfates (which are prevalent in conventional pulverized coal-fired boilers) and by increased mobility of corrosion-accelerating agents in the deposit layers due to the much higher temperature of the heat transfer surfaces in the HIPPS. It is major challenge to develop methods to combat severe deposition, erosion, and corrosion of heat transfer surfaces that are exposed to higher-than-normal temperatures. These methods could include fuel selection, cleaning of aggressive contaminants from coal, fine grinding of coal, use of additives, and selection of advanced corrosion-resistant ceramic materials, coatings, and advanced alloys for vulnerable heat transfer sections.

In earlier studies, several ceramic materials were examined to evaluate their performance after exposure to dry air, salt environments that contained Na_2SO_4 or a 75 wt.% Na_2SO_4-25 wt.% NaCl mixture, and three coal slags that simulated slags obtained from combustion of coals from eastern and western U.S.[3-5] The results showed that the materials exposed to an air environment undergo passive oxidation of SiC to SiO_2. Exposure of these materials to salt environments led to catastrophic corrosion, especially if the sodium activity of the condensed salt was high, by enabling formation of low-melting corrosion products. The mode of degradation of SiC-based materials involves reactions between the ceramic materials and alkali sulfates such as Na_2SO_4 and K_2SO_4, and alkali chlorides such as NaCl and KCl. In the combustion gas environment, the concentrations of oxygen and of sulfur as SO_2 and SO_3 determine the sodium oxide activity via the reaction $Na_2SO_4 = Na_2O + SO_3$. Subsequently, the silica phase that forms on the ceramic materials reacts with Na_2O to form compounds such as $Na_2O \cdot XSiO_2$, where X can be 0.5, 1, 2, or 4. These sodium silicates exhibit melting temperatures of 875-1110°C. This mode of degradation of ceramic materials requires sufficiently high Na_2O activity and is usually possible in gas turbine systems where slag constituents are virtually absent. In such instances, the liquid phase can dissolve the protective SiO_2 scale and also cause the liquid reaction products to penetrate into the substrate ceramic material and thereby mechanically weaken the material.

In coal-fired combustion systems, the presence of slag constituents determines the thermodynamic activity of various deposit constituents, and alkali-sulfate-induced corrosion is generally not dominant. The mode of degradation of ceramic materials in coal-fired combustion systems is via reactions with coal ash. This type of degradation depends on material composition, slag chemistry (acidic or basic), and gas-phase environment (either oxidizing or reducing). The slags generally contain phases such as SiO_2, Al_2O_3, CaO, Fe_2O_3, Na_2O, a combination of these phases, and other ash constituents, depending on the coal feedstock. X-ray diffraction (XRD) data for deposits, that were obtained during a Combustion and Environmental Research Facility (CERF) run with combustion of Pittsburgh coal showed the dominant phases to be mullite

($3Al_2O_3 \cdot 2SiO_2$), ordered calcian albite ([Na,Ca] Al $[Si,Al]_3O_8$), and hematite (Fe_2O_3). The melting temperatures of these phases are >1400°C; reactions between these compounds and the ceramic materials occur primarily in the solid state, and little or no penetration of the ceramics by liquid phase from coal combustion environment occurs.

Similarly, XRD data for the deposits, obtained during a CERF run with combustion of Alaskan/Russian blend coal, showed the dominant phases to be anorthite ($CaO \cdot Al_2O_3 \cdot 2SiO_2$), calcium aluminum silicate ($CaO \cdot Al_2O_3 \cdot SiO_2$), and ordered sodium anorthite (Ca,Na) $(Al,Si)_2$ Si_2O_8. These calcium-rich silicates also have melting temperatures >1400°C, and reactions between the coal ash deposit and the ceramics occur predominantly in the solid state. The experimental results also indicate that Na_2O activity in the deposits (with combustion of coals that contain Fe_2O_3 and CaO) is sufficiently low to form liquid sodium silicates of various types in coal-fired systems.

On the other hand, exposure of the materials to slags obtained from typical coal ashes had very little effect on the corrosion performance of the materials, especially at 1200°C, where the reactions do not involve formation of liquid corrosion products. Four-point bend tests, conducted on several of the materials after exposure to dry air, salt, and slag environments, indicated that sodium salts (both sulfates and chlorides) have the greatest degrading effect on corrosion properties of the materials, whereas exposures to air and slag environments had minimal effect on the properties at 1200°C.

The objectives of the work presented here were to (a) evaluate the influence of water vapor in the environment on the oxidation behavior of SiC-based materials, (2) assess the effect(s) of simultaneous presence of coal slag and combustion gas (with water vapor) on the corrosion behavior of materials, and (c) determine the residual mechanical properties of the materials after exposure to the above-mentioned environments.

EXPERIMENTAL PROCEDURE

Materials

The materials selected for the laboratory experimental program include monolithic ceramic materials and ceramic-matrix ceramic composites.

Sintered alpha SiC is a fully densified (>98% of theoretical density) ceramic material produced by sintering. It is a single-phase material that has a very fine grain structure (8 μm) for excellent wear resistance, contains no free silicon, and has been reported to be chemically resistant in both oxidizing and reducing environments. The density of this material is ≈3.1 g/cm^3.

SiC in a silicon matrix is a material that consists of silicon carbide in a silicon matrix. The silicon metal phase provides good fracture toughness and resistance to thermal shock, oxidation, and creep without the extreme brittleness of many ceramic materials. The material exhibits a density of 2.8 g/cm^3, 0% porosity, and contains ≈47% silicon.

Siliconized SiC consists of 90 vol.% SiC, 8 vol.%Si metal, and 2 vol.% pores. The material has a density of 3.1 g/cm^3.

The SiC(f)/SiC matrix material contains ≈40 vol.% SiC fibers (criss crossed in two dimensions) in a SiC matrix with a 10 vol% porosity. The density of the material is 2.5 g/cm^3 and it exhibits excellent compressive and interlamellar shear strength, high stiffness, and good oxidation resistance.

SiC(p) in Al_2O_3 is a composite material that contains SiC particulates in an alumina matrix. The material contains some free aluminum in the matrix becausee the material is made by direct metal oxidation. The material combines the thermal properties of SiC and corrosion resistance of alumina. Particulate loading is in the range of 50-55 vol.%; particle diameter is 5-20 µm. The material contains ≈40 vol.% alumina, ≈10 vol.% Al, and 1 vol.% of ores.

Oxidation and Corrosion Tests

Coupon specimen 25.4 x 4.76 x 1.6 mm were prepared from several of the above–listed materials for oxidation experiments at 1000, 1200, and 1400°C in dry air. In addition, experiments were performed at 1200°C in air that contained water vapor. Dimensions and initial weights of the specimens were measured prior to exposure. Before the oxidation treatment, all but the SiC(f)/SiC specimens were ground on 1200-grit SiC paper and cleaned with alcohol. The specimens were placed in an alumina holder that was suspended into an alumina chamber inside a resistance-wound furnace. The heating was conducted at a rate of 5°C/min in the exposure environment. Water vapor was introduced into the air stream by passing the air through a heated water bath. In this study, the air was saturated with water at 46 and 69°C, which resulted in 10 and 30 vol.% water vapor in the air, respectively. Each experimental series consisted of five cycles of 100 h each. An electrobalance with a sensitivity of 0.1 mg was used after each cycle to determine weight change of the specimens that was due to oxidation.

Exposures in the presence of three slags were conducted at 1200°C for 200 h. Table 1 lists the compositions of the slags and the coals that were combusted to obtain these slags. Analysis shows that the slag obtained from Illinois #6 coal was richer in Fe_2O_3 and leaner in CaO and MgO, whereas the reverse was seen for slag from Rochelle coal. Slags #43 and XX typify the slags derived from coals in the eastern U.S., whereas the slag #47 is typical of that derived from western coals. Slag exposure tests were conducted in a flowing gas mixture of air-1 vol.% SO_2 with and without 10 vol.% water vapor.

Table 1. Compositions of slags for laboratory study

Compound	Slag 43/ Illinois #6	Slag 47/ Rochelle	Slag XX/ Illinois #6
SiO_2	52.9	47.1	53.3
Al_2O_3	16.6	18.8	18.6
Fe_2O_3	12.9	5.2	17.6
CaO	13.0	19.6	7.2
MgO	1.3	5.8	1.0
Na_2O	0.8	0.9	0
K_2O	1.6	0.3	1.7
SO_3	0.1	0.3	0

Mechanical Tests

The effect of air oxidation, water vapor additions, and exposures to slag from Illinois #6 and Rochelle coals on the flexural strength of four candidate materials was evaluated by preexposure to the specific environment and postexposure four-point bend testing of the specimens in vacuum. For these evaluations, the temperature was maintained at 1200°C during both the preexposure and the mechanical testing. The flexural test involved bending a specimen of rectangular cross section until fracture. The specimen dimensions were 25.4 x 4.76 x 1.6 mm and the slag-exposed surface was maintained under tension during the test. The data on the load that was necessary to cause fracture and the area under the load-displacement curves were used to calculate the flexural strength of the material and the energy absorbed during the fracture.

Microstructural analysis

Upon completion of the oxidation experiments, slag exposures, and mechanical testing, fracture surfaces and polished cross sections of several of the specimens were analyzed by scanning electron microscopy (SEM), energy dispersive X-ray (EDX) analysis, and XRD.

EXPERIMENTAL RESULTS

Oxidation in Dry and Wet Air

Oxidation of ceramic materials, such as monolithic and composite SiC and SiC-dispersed Al_2O_3, involves reaction of carbide phases to silicon-rich oxides. The rate of oxidation is generally influenced by the porosity of the material, the amount of free silicon and/or aluminum in the material, and exposure temperature. Earlier work showed a low rate of oxidation for these materials when exposed in dry air at 1200°C.[4,5] One exception was SiC(p) in Al_2O_3 material, which exhibited a large increase in weight gain in the early stage of exposure, due to oxidation of free aluminum in the surface region of the sample. After ≈100 h of exposure, the oxidation rate slowed but was still higher than in other materials, indicating oxidation of free aluminum in the interior of the material, dictated by the diffusion of oxygen. The results also established that these ceramic materials undergo passive oxidation at temperatures in the range of 1000-1400°C in a dry-air environment.

Figure 1 shows weight-change-versus-time data for specimens of several ceramic materials exposed to air with 0, 10, and 30 vol.% water vapor at 1200°C. It is generally accepted that during oxidation of silicon-based materials, the mobile species is oxygen and not silicon. Several reactions are possible for the oxidation of SiC to SiO_2:

$$SiC + 3/2\ O_2 = SiO_2 + CO \quad (1)$$

$$SiC + O_2 = SiO(g) + CO \quad (2)$$

$$SiC + O_2 = SiO_2 + C \quad (3)$$

$$SiC + 2\ O_2 = SiO_2 + CO_2 \quad (4)$$

$$SiC + 2\ H_2O = SiO_2 + C + 2\ H_2 \quad (5)$$

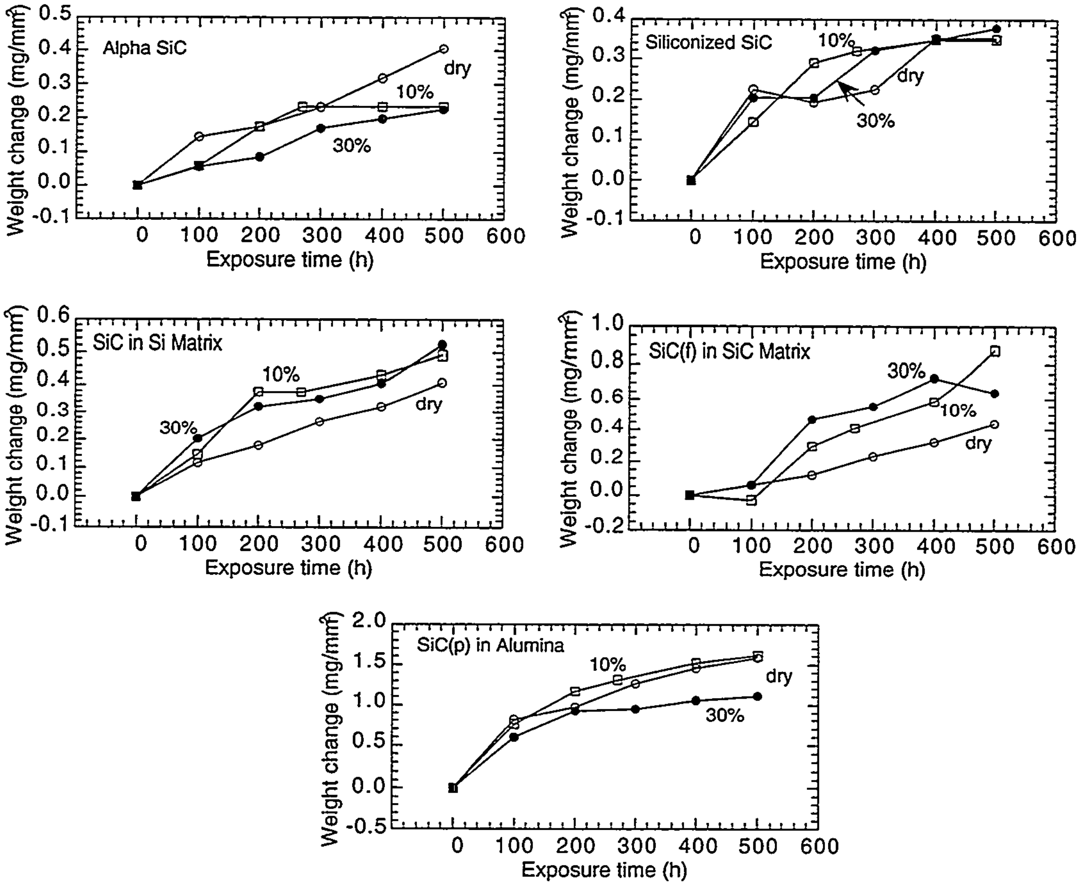

Figure 1. Influence of water vapor on the oxidation performance of several SiC-containing materials

All of the listed reactions are thermodynamically favored, but the kinetics of these reactions are dictated primarily by temperature. Uncertainties, however, exist as to whether molecular oxygen diffuses through silica scale or if oxygen ion diffusion is the rate determining step. At 1200°C in an air environment with and without water vapor, reaction 2 was not observed because the vapor pressure of SiO is negligible. Furthermore, the kinetics of carbide oxidation are influenced by the rate of transport of CO and/or CO_2 through the silica scale, because the new oxide generally grows on the SiC/SiO_2 side of the interface. The kinetics of reaction 3 are dictated by the oxygen transport through silica scale and lead to carbon deposition. None of the ceramic materials examined in the present work showed a significant influence of water vapor partial pressure on the oxidation rate at 1200°C. The oxidation rates of alpha SiC (with no free silicon and ≈0% porosity) and siliconized SiC (with 8% free silicon and 2% porosity) in air with and without water vapor are similar. SiC in a silicon matrix (47% free silicon and no porosity) showed a slight increase in absolute weight gain but the oxidation rate was similar in dry air and in air with water vapor. Only the fiber-reinforced SiC material (with 10% porosity) showed a slight increase in oxidation rate when air contained 10 vol.% water vapor. The increase in water vapor content up to 30 vol.% did not further enhance the oxidation rate at 1200°C. Extensive microstructural analysis of oxidized specimens showed a continuous silica scale on all of the specimens and the thickness of oxide scale was similar for specimens exposed in dry air and in air that contained 10 and 30 vol.% water vapor (see Fig. 2, typical of monolithic materials). Only the fiber-reinforced SiC material became thicker with an increase in water vapor content (see Fig. 3).

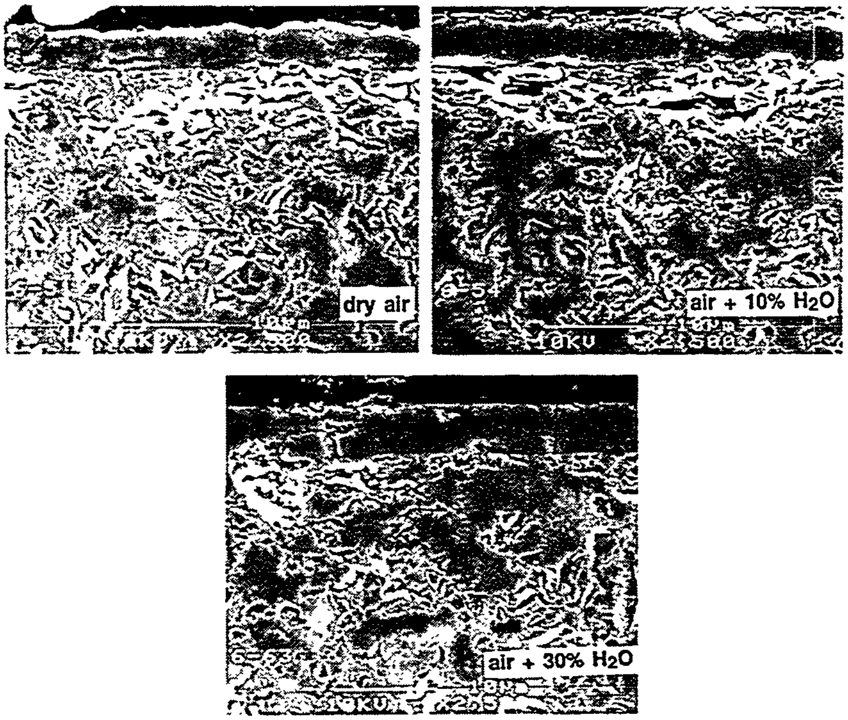

Figure 2. Scanning electron photomicrographs of cross sections of siliconized SiC material after 500-h exposure at 1200°C in dry air and in air that contained 10 and 30 vol.% water vapor

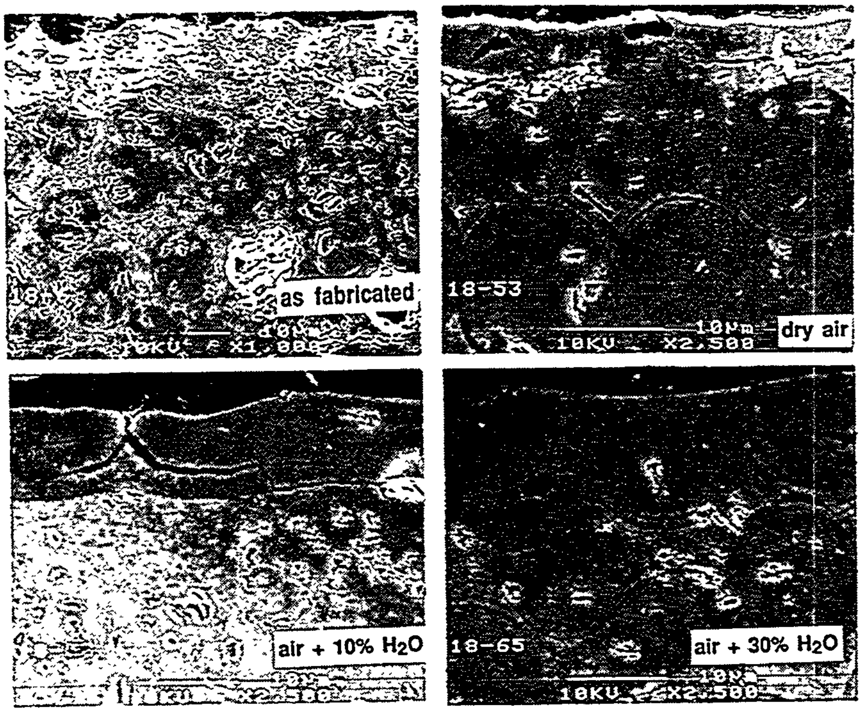

Figure 3. Scanning electron photomicrographs of cross sections of SiC(f)/ SiC matrix material in as-fabricated condition and after 500-h exposure at 1200°C in dry air and in air that contained 10 and 30 vol.% water vapor

Exposure in Slag Environments

In laboratory slag tests, specimens showed significant surface cracking but the slag itself did not seem to penetrate the specimens, as indicated by EDX analysis of specimen cross sections. Because Na_2O activity in the slag is relatively low, the deposit did not melt, but significant bubbling of the slag, probably due to evolution of CO and CO_2, was noted. All three slags exhibited a similar appearance after the test and all three specimens exposed to differing slags also appeared similar, indicating that coal slag chemistry has little influence during these short (200-h) exposures. During the CERF exposure conducted with Pittsburgh coal, the specimen exhibited a thin layer of deposit after ≈100 h of testing. X-ray diffraction analysis of the deposit indicated predominantly mullite ($3Al_2O_3 \cdot 2SiO_2$), with some ordered albite ($[Na,Ca]Al[Si,Al]_3O_8$) and traces of hematite. No significant degradation of the sample was observed by SEM and EDX analysis. During the CERF exposure conducted with Alaskan/Russian coal, the dominant phases were anorthite ($CaO \cdot Al_2O_3 \cdot 2SiO_2$), calcium aluminum silicate ($CaO \cdot Al_2O_3 \cdot SiO_2$), and ordered sodium anorthite $(Ca,Na)(Al,Si)_2 Si_2O_8$. The melting temperatures of these calcium-rich silicates are also >1400°C, and reactions between the coal ash deposit and the ceramics occur predominantly in the solid state. The experimental results also indicate that Na_2O activities in the deposits (with combustion of coals that contain Fe_2O_3 and CaO) are sufficiently low to form liquid sodium silicates of various types in coal-fired systems.

Tests were also conducted at 1200°C to evaluate the combined effect of slag and simulated combustion gas with water vapor on corrosion of the materials. Analysis of cross sections of exposed specimens showed similar scale morphologies; the oxide layer thickness was slightly greater for the specimen exposed in a

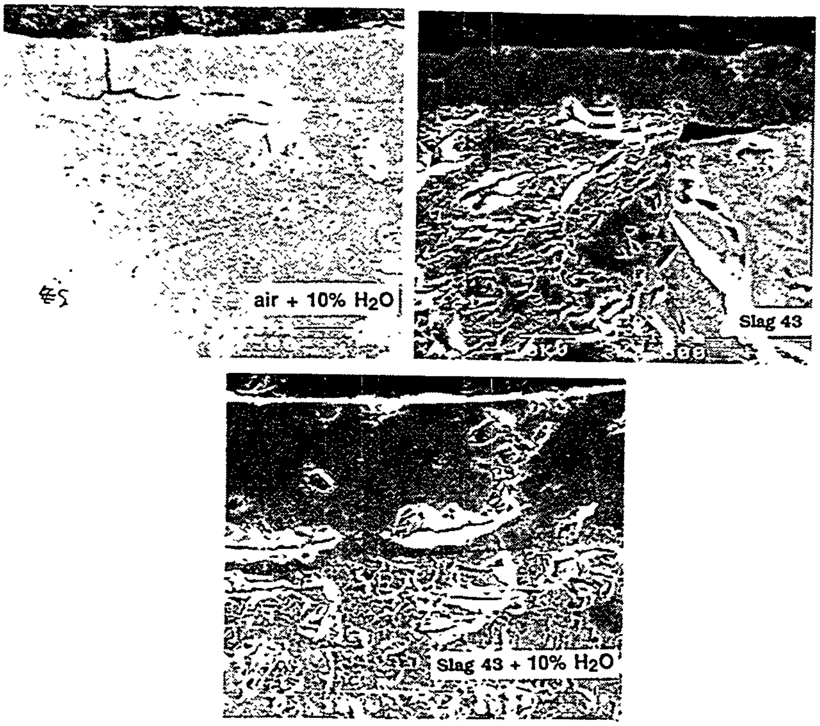

Figure 4. Scanning electron photomicrographs of cross sections of SiC in Si matrix material after 200-h exposure at 1200°C in environments of air with 10% water vapor and slag 43 with and without 10% water vapor

combined environment of slag and 10 vol.% water vapor than those obtained in either of them alone (see Fig. 4 for a specimen of SiC in a silicon matrix). At present, data are not adequate to quantify the relative effects of water vapor and slag on the scaling kinetics of these materials.

Four-Point Bend Test Data

Four-point bend tests were conducted on all of the materials at 1000, 1200, and 1400°C. The load that was necessary to cause fracture in the test was used in the following expression to calculate the flexural strength of the materials:

$$\sigma = \frac{3(L_1 - L_2)P}{2\,t^2\,w},$$

where σ is flexural strength in MPa; L_1 and L_2 are distances between support points and load points, respectively; P is load; and t and w are thickness and width of the specimen, respectively. Data obtained on the flexural strength of the materials and energy absorbed by the materials during fracture were reported earlier.[4,5]

To examine the role of exposure environment on mechanical properties, several specimens of the ceramic materials were preexposed for 200 h at 1200°C to dry air with and without water vapor, to three coal slags, identified as 43, 47, and XX, and to simulated combustion gas with and without water vapor. After exposure, the specimens were mechanically tested in vacuum at 1200°C. During these tests, the specimen surfaces exposed to the slag environments were on the support side of the fixture, ensuring a tensile mode of loading for the surfaces exposed to corrosive environments.

Figure 5 shows the flexural strength of the four materials in as-received condition and after exposure to dry air with and without water vapor. It is evident that exposures of 500 h in differing environments had little influence on the strength of all but the fiber-reinforced composite material. Analysis of fracture surfaces of exposed specimens showed formation of thin layers of silica during exposure to air. Figure 6 shows the flexural strength of the four materials after 200 h of exposure to three slags with and without water vapor. The results show that the strength of the alpha SiC and SiC in silicon-matrix materials with almost no porosity differed negligibly after exposure to environments with and without water vapor. This finding also indicates that the flexural strength of the material with a free silicon content of 47% is inherently lower and oxidation/corrosion is not of concern, based on these short exposure tests. Siliconized SiC (with 8% free Si and 2% porosity) and SiC(p) in alumina (with 10% Al and 1% porosity) showed substantial increase in flexural strength in the presence of water vapor when compared with strength of specimens exposed to an environment without water vapor. The bend-tested specimens are currently being analyzed to examine the oxidation/corrosion-product phases and to determine the cause of the noted increase in strength.

SUMMARY

Several monolithic and composite ceramic materials have been evaluated for their corrosion resistance in environments of interest in advanced combustion systems. Oxidation of these materials in air is in "passive" mode and leads to formation of silica only. Water vapor contents up to 30 vol.% in air had minimal effect on the oxidation rate of these materials at 1200°C and exposure to slag environments at 1200°C showed minimal attack, primarily due to the absence of liquid corrosive products. Exposure of these

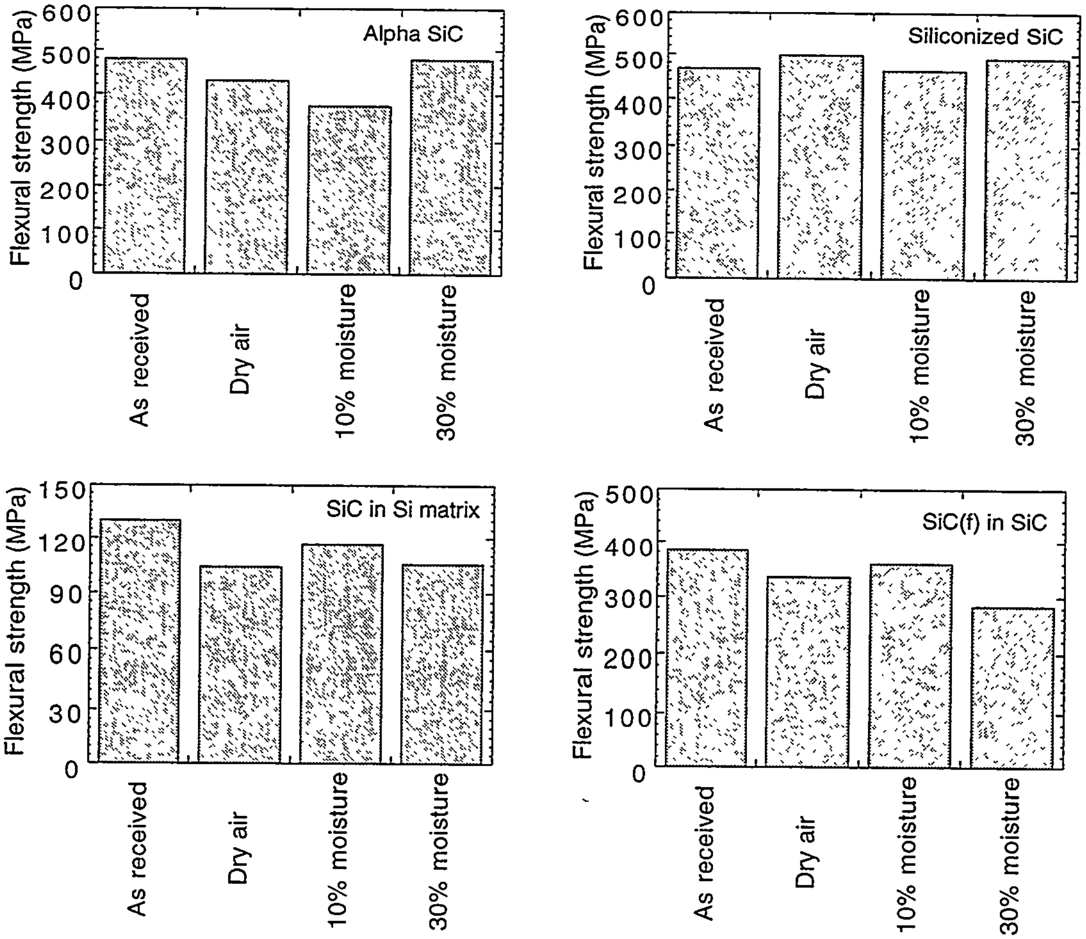

Figure 5. Effect of 500-h exposure in differing environments at 1200°C on flexural strength of several SiC-based materials

materials in coal-fired combustor experiments showed deposits rich in mullite (silica-alumina phase) and anorthite (calcia-silica-alumina phase), both of which have melting temperatures >1400°C.

Four-point bend test data showed that air oxidation up to 500 h at 1200°C had minimal effect on strength properties; tests showed minimal effect of water vapor on strength of alpha-SiC and siliconized SiC. Some strength reduction was evident in the SiC(f)/SiC matrix material; this may be due to a greater porosity of this material. Free carbon detected on the fracture surface may be deleterious over the long term. Exposure to any of the three slags had a negligible effect on the flexural strength of the materials; in the presence of slag and simulated combustion gas that contained water vapor, porous materials such as siliconized SiC and SiC(p) in Al_2O_3 showed improvement in flexure strength.

ACKNOWLEDGMENTS

This work was supported by the U.S. Department of Energy, Office of Fossil Energy, Advanced Research and Special Technologies Materials Program. The assistance of M. Mathur and M. Freeman of the

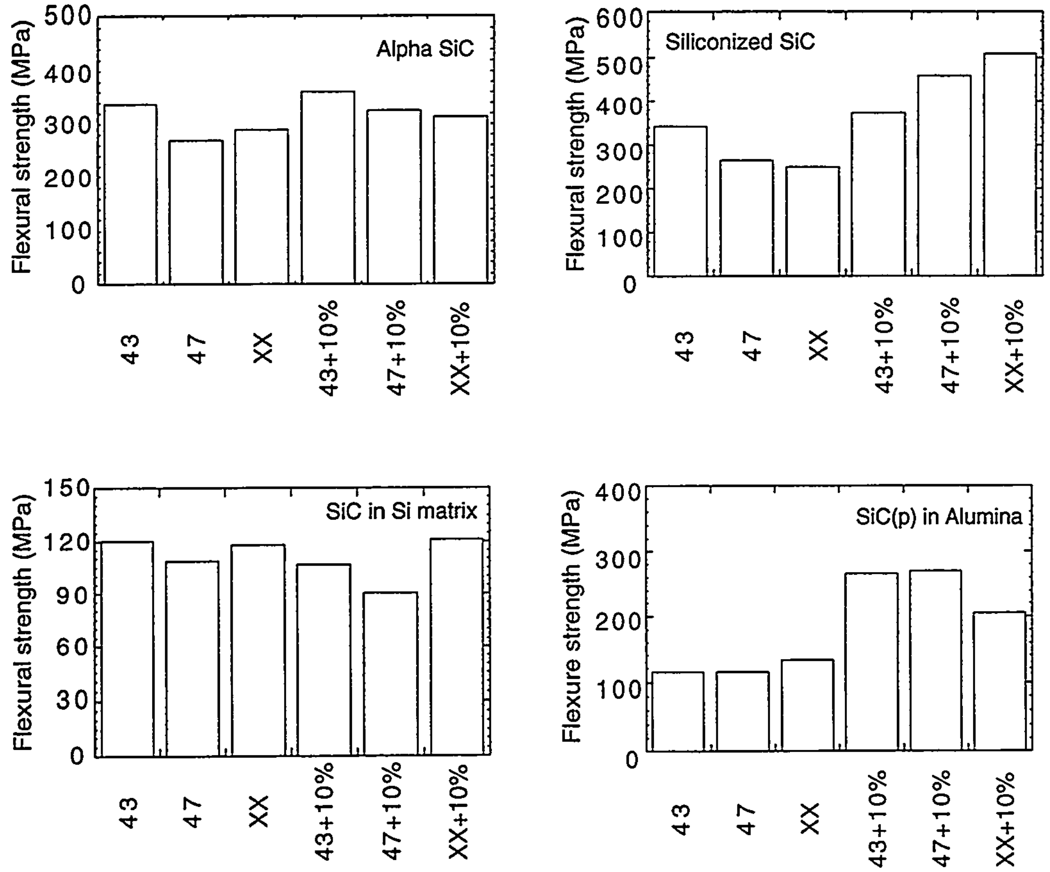

Figure 6. Effect of 200-h exposure in various slag-containing environments at 1200°C on flexural strength of several ceramic materials

Federal Energy Technology Center in the conduct of exposures in CERF is gratefully acknowledged. D. L. Rink assisted in the corrosion and four-point bend tests and microstructural analysis of exposed specimens.

REFERENCES

1. L. A. Ruth, "Combustion 2000," PETC Review, Issue 4, p. 4, Fall 1991.
2. K. Natesan, M. Yanez-Herrero, and C. Fornasieri, "Corrosion Performance of Materials for Advanced Combustion Systems," Argonne National Laboratory Report ANL/FE-93/1, 1993.
3. K. Natesan, M. Freeman, and M. Mathur, "Corrosion Performance of Materials for Advanced Combustion Systems," Proc. 9th Annual Conference on Fossil Energy Materials, ORNL/FMP-95/1, p. 71, 1995.
4. K. Natesan, "Corrosion and Its Effect on mechanical properties of Materials for Advanced Combustion Systems," Proc. 10th Annual Conference on Fossil Energy Materials, ORNL/FMP-96/1, p. 63, 1996.
5. K. Natesan, "Corrosion Performance of Ceramic Materials in Slagging Environments," NACE CORROSION/97 Conference, New Orleans, LA, March 9-14, Paper #143, 1997.

EVALUATION OF AN ALL-CERAMIC TUBESHEET ASSEMBLY FOR A HOT GAS FILTER

J. L. Bitner

Mallett Technology, Inc.
121 Hillpointe Dr., Suite 300
Canonsburg, PA 15317-9502

R. H. Mallett

Mallett Technology, Inc.
P. O. Box 14407
Research Triangle Park, NC 27709-4407

P. M. Eggerstedt

Industrial Filter & Pump Mfg. Co.
5900 Ogden Avenue
Cicero, IL 60650-3888

R. W. Swindeman

Oak Ridge National Laboratory
P.O. Box 2008
Oak Ridge, TN 37831-6084

ABSTRACT

A 10-inch thick, all-ceramic tubesheet design is evaluated for differential pressure and thermal conditions. Primary stresses from differential pressure are well within a safe allowable. The calculated peak thermal stresses at local discontinuities approach the modules of rupture for the ceramic material. Kiln tests were performed to demonstrate differential temperatures between hot center and cooler rim do not cause failures or visible tensile cracks. There appear to be mitigating mechanisms and design features in the Industrial Filter & Pump (IF&P) Mfg. Co. all-ceramic tubesheet design concept that add forgiveness in accommodating differential pressure and thermal loading stresses. A material characterization program on the ceramic materials is recommended.

INTRODUCTION

An all-ceramic tubesheet for the IF&P hot-gas filter is evaluated for thermal and structural conditions defined for the transport combustor demonstration plant at the Southern Company Services facility in Wilsonville, Alabama.[1] The all-ceramic tubesheet assembly provides support for the primary and safety ceramic candle filters that are used to remove the ash particulate from the hot gas, separates the filtered gas chamber from the unfiltered chamber and reacts the differential pressure caused by pressure drop through the filtering assembly. To simplify the analysis, bounding evaluations are performed in accordance with the IF&P design specification for the tubesheet assemblies.[2] The deterministic evaluations are based upon thermal and structural finite element analyses performed using the ANSYS® computer program.

GEOMETRY AND MATERIAL PROPERTIES

The geometry used in this all-ceramic tubesheet evaluation is from drawings given in the analysis specification for the IF&P filter design.[2]

The typical Fibroplate™ 2600 II ceramic material properties used in this evaluation are:

Modulus of Elasticity (E) = 2×10^6 psi
Poisson's Ratio (ν) = 0.13
Coefficient of Thermal Expansion (α) = 3.3×10^{-6} in/in-°F
Mass Density (ρ) = 0.144 lb-hr^2/in^4
Thermal Conductivity (k) = 0.0939 Btu/hr-in-°F
Specific Heat (c) = 0.13×10^{10} Btu-in/lb-hr^2-°F

As specified in the design analysis specification, temperature dependence for these properties is considered in the evaluation. The source of the properties is defined in the design analysis specification.[2]

ANALYTICAL MODELS

Three separate analysis models are used in the evaluation. The first model is an axisymmetric model shown in Figures 1 and 2. Figure 1 shows both the structural and insulation materials. Figure 2 shows only the structural components and the finite element grid.

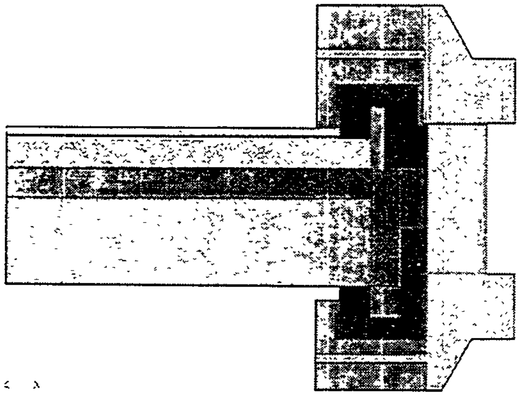

Figure 1 — Axisymmetric Model - All Materials

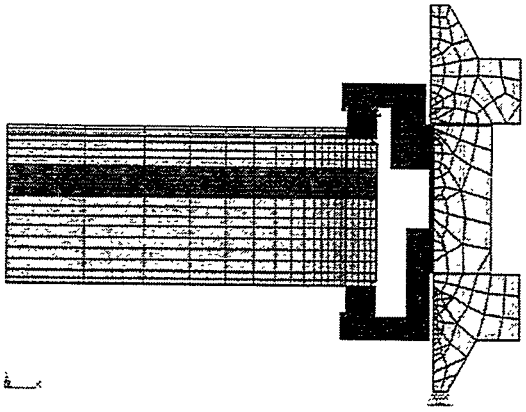

Figure 2 — Axisymmetric Model - Structural

This model is by far the most valuable in evaluating the design of the ceramic layers of the tubesheet assemblies. Other models are needed to address the tubesheet segmented support components and candle hole discontinuities. The temperatures predicted using this axisymmetric model are applicable to all components of the assembly including the tubesheet supports and the pressure vessel. The stresses predicted for the tubesheet assemblies are also applicable except in the vicinity of local geometric effects where appropriate stress concentration factors must be applied.

The second analysis model used in the evaluation is a sector model shown in Figure 3. The purpose of the sector is to examine the effects of segmenting the metallic support ring and hold down rings. The axisymmetric model includes an artificial hoop stress in the segmented rings which is not present in this sector analysis model.

The third analysis model shown in Figure 4 is used in the evaluation to determine the stress concentration effects of the hole pattern for the filter candles. The model encompasses a typical hole pattern in a ceramic plate. Stress concentration factors are determined under differential pressure loading and rim pressure loading. These stress concentration factors are applied to the stresses obtained using the axisymmetric model for predicting the stresses in the vicinity of the holes.

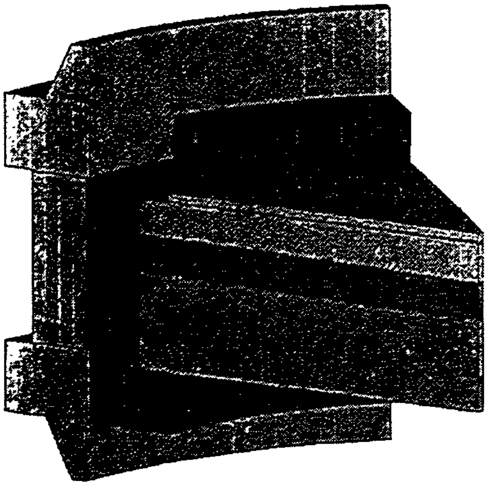

Figure 3 — Sector Model - Structural

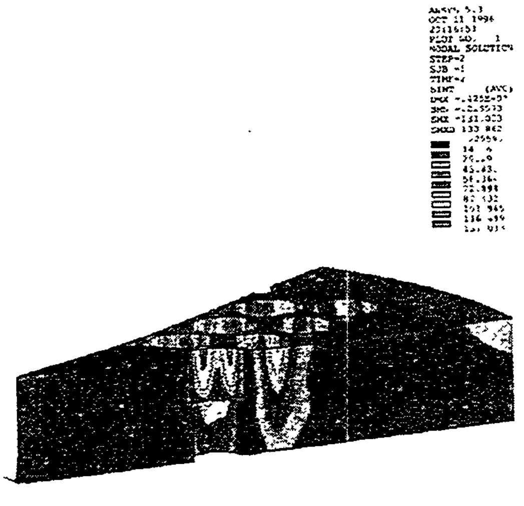

Figure 4 — Plate Model - With Holes
Rim Pressure - Stress Intensity

LOADING CONDITIONS

The loading conditions that are used in the evaluation are defined in the design analysis specification.[2] To keep the specific analysis cases to a manageable number, bounding cases are used. The two main bounding design conditions evaluated are the design differential pressure of 15 psi and design steady state temperature of 1,800 °F. Both of these values are extremely conservative since the normal operating pressure is expected to be 2 or 3 psi at a temperature between 1,200 - 1,400 °F,

ANALYSIS PROCEDURE

The finite element analysis method is used in this investigation. Calculations are performed using the ANSYS® computer program and the analytical models defined in the preceding section.[3] Quadratic finite elements with mid-side nodes are used for all models for both thermal and structural analyses. Refinement is set to obtain accurate results commensurate with features of the component being examined.

The challenges of the analysis models lie in determining the local effects within an overall model and in representing the interactions among the several components. The challenge of local effects is addressed by using several different models. The axisymmetric model is used to determine the response of the tubesheet with a simplified support structure model. The sector model is used to determine the response of the support structure with a simplified tubesheet model.

The challenge of addressing interaction effects between components is met by using alternative assumptions. For example, the tubesheet is not only analyzed as a single integral component but also as two disconnected components including the effects of contact between the components. The support rings are analyzed as being completely connected and as being loosely connected.

The thermal analysis procedures are nonlinear because of the dependence of material properties upon temperature. The structural analyses are nonlinear because the footprint of contact between parts is not known apriori. These nonlinearities require iterations which increase the calculation effort beyond that needed for linear analysis.

The greatest uncertainties in the tubesheet analysis are in the material properties needed to predict behavior and those needed to evaluate the structural integrity based upon the predicted behavior. The approximations in the analysis models and analysis procedures are judged to be acceptable considering the uncertainties in material properties and applied loading. After reviewing the design geometry, material properties and loading conditions in relation to the analysis results, more refined analyses that focus on localized strains and operational thermal transients may be appropriate to build confidence in the integrity of the design.

RESULTS

Axisymmetric Model

Thermal — The predicted steady state temperature distribution is shown in the temperature contour plot of Figure 5. The temperature of the ceramic tubesheet is nearly equal to the hot gas temperature of 1,800 °F.

The maximum temperature of the outside surface of the vessel in the vicinity of the insert ring is less than 200 °F for an ambient temperature of 70 °F. The minimum surface temperature in the flange region is 158 °F.

There is a cutout in the insulation at the bottom of the tubesheet which permits exposure of hot gas to the inside diameter of the Marinite™ ring. The top Marinite™ ring is embedded in the insulation. This difference in insulation leads to a difference in temperature of the upper and lower corners of the tubesheet components. Based upon this difference, a higher thermal stress in the upper corner is anticipated during normal operation. The main temperature gradient occurs across the segmented Marinite™ rings. The lower Marinite™ ring ranges from 1,734 °F to 693 °F. The upper Marinite™ ring ranges from 1,310 °F to 483 °F.

The key indication of thermal stress in the tubesheet of Figure 6 is the differential temperature between the hot interior and the cooler rim of the tubesheet. Below the flow block interface (to the right in Figure 6), the minimum temperature at the rim of the tubesheet is 1,450 °F. Above the flow block interface the minimum temperature at the rim of the tubesheet is 1,227 °F.

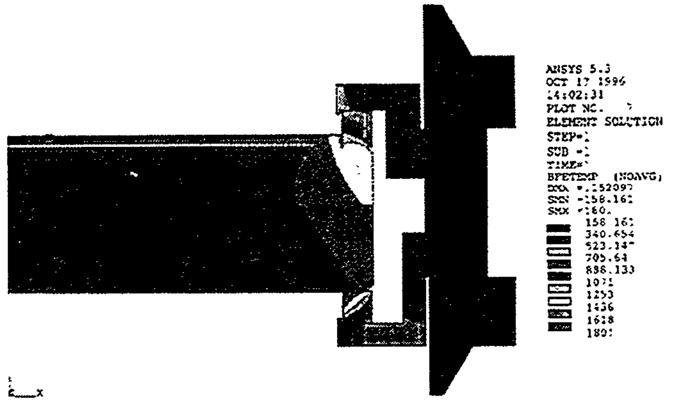

Figure 5 — Axisymmetric Model - Temperature

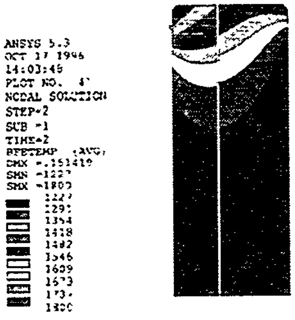

Figure 6 — Axisymmetric Model - Tubesheet - Temperature

Stress — For evaluating stresses two cases were examined. Analysis Case A1 specifies an integral connection across the flow block interface. This assumes that the bolts which connect the layers of the tubesheet are fully effective in making the two tubesheet assemblies respond as a single layer. Analysis Case A2 assumes the bolts are ineffective and the two tubesheet assemblies respond independently.

Case A1 shows high hoop tension exists in the relatively cool rim of the tubesheet. The maximum value in the upper tubesheet assembly is 3,350 psi. The maximum hoop tension in the lower tubesheet assembly is 2,181 psi. The compressive stress in the central region of the tubesheet reaches -618 psi. The maximum hoop stresses are approximately the same for Case A2; but, the compression in the central region reaches -847 psi. For Case A1, the maximum through-thickness axial compressive stress is -916 psi in the tubesheet caused by the squeeze between the support rings and by the 15 psi differential pressure. For the combined steady state thermal and differential pressure loading, the maximum stress is 4,064 psi. The hoop stress is the dominant stress component. Similar results are obtained for Case A2.

For the 15 psi upward differential pressure only, the important stress values are the hoop stresses on the top and bottom in the central region. The maximum compressive stress on the bottom is 95 psi. The maximum tensile stress in the central region of the top is about the same.

The Case A2 structural results for the thermal-plus-structural loading are essentially the same as for Case A1. The tubesheet results for only pressure loading are quite different. The key results of Case A2 are the hoop stress distributions shown in Figure 7. The lower tubesheet assembly has hoop stress in the central region which varies from -148 psi to +119 psi. The upper tubesheet assembly has hoop stress that varies in the central region from -147 psi to 153 psi.

Sector Model

Thermal — The thermal results for the sector model are essentially the same as for the axisymmetric model. The overall temperature distribution at steady state conditions is shown in Figure 8.

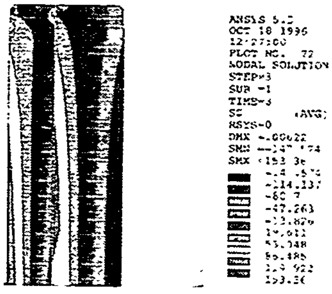

Figure 7 — Axisymmetric Model - Tubesheet - Pressure - Hoop Stress

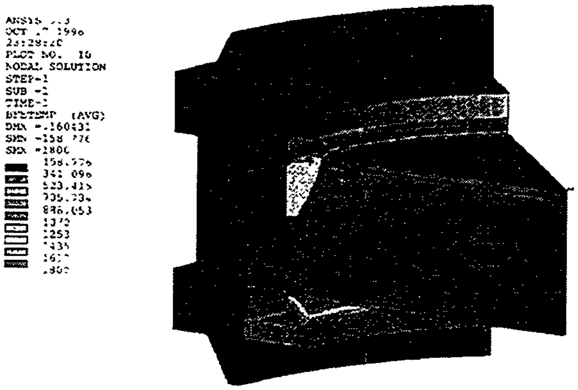

Figure 8 — Sector Model - Steady State Temperature

Stress — Two analysis cases are addressed. Case S1 is comparable to Case A1 except that the components of the support structure are segmented appropriately in Case S1. In Case A1, all components are considered to be full 360° axisymmetric rings. In Case S1, the segmented ring components are assumed to be integrally connected by the bolts and to act as a single unit. An additional Case S2 was constructed to obtain results corresponding to loosely connected ring segments.

The results for Cases S1 and S2 are for steady state thermal loading plus 15 psi differential pressure. The thermal effects are dominant. Figure 9 shows the hoop stress distribution on the symmetry plane for Case S2.

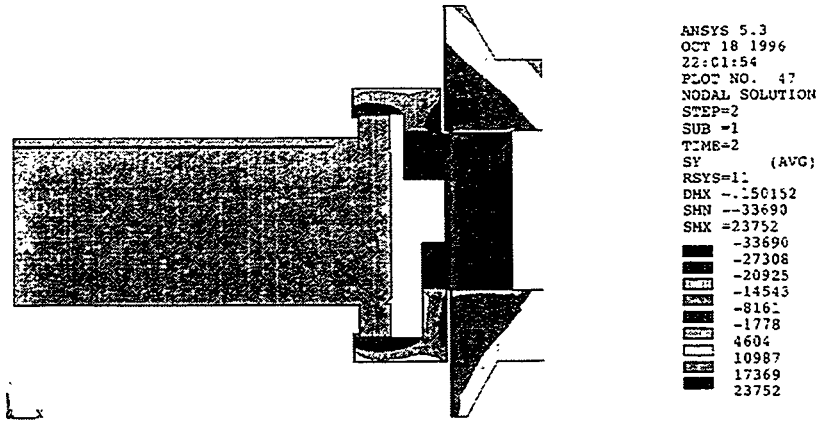

Figure 9 — Case S2 Symmetry Plane Sector Model
- Temperature + Pressure Hoop Stress

The hoop stress in the lower support ring for Case S1 shows strong bending from inside (-74,995 psi) to outside (+8,472 psi). When changed from integral to loose connection, the results show greater bending from top (-22,589 psi) to bottom (+11,955 psi) along the support platform. The maximum stress intensity of 22,445 psi indicates that hoop stress is the dominant stress component.

The hoop stress in the hold down ring segment for Case S1 shows strong bending from inside (-24,670 psi) to outside (-7,554 psi). The hot tip creates a force which bends the back plane. When changed from integral to loose connection, the results show bending from bottom (-13,767 psi) to top (7,878 psi) along the hold down platform. The maximum stress intensity of (13,763 psi) again shows that hoop stress is the dominant stress component.

Ligament Model

The overall distribution of stress intensity in the ligament model from a 15 psi pressure over the bottom surface is shown in Figure 4. These intensified results are compared to the corresponding results for the case of a tubesheet without holes to obtain a stress intensification factor. The maximum stress intensity in the tubesheet with holes is 1,232 psi at a radius of 10 inches. The stress at this location without holes is 285 psi. The stress intensity factor (sif) caused by the candle filter holes is $k_p = 1{,}232/285 = 4.3$ at the maximum stress location under differential pressure.

The overall distribution of stress intensity in the ligament model due to a 15 psi radial pressure over the outer radial surface is also determined and compared to the corresponding results for the case of a tubesheet without holes for the filter candle such as was used in the axisymmetric model of the tubesheet. The maximum stress intensity in the tubesheet with holes is 131 psi at a radius of 10 inches. The stress intensity in this location without holes is 15 psi. The stress intensity factor (sif) caused by the candle filter holes is $k_t = 131/15 = 8.7$ at the maximum stress location under radial rim pressure.

The results of the finite element analysis for the ceramic tubesheet are summarized in Table 1 in terms of hoop stress component which dominates and is nearly equal to the stress intensity. In the absence of thermal stresses, the design of the ceramic tubesheet is clearly satisfactory especially considering the normal operational differential pressure is not expected to exceed 2 or 3 psi.

Table 1 — Hoop Stress Summary

Tubesheet Assembly	Loading	Temperature °F	Max Hoop Stress (psi)		Allowable (From Spec[2])
			Nominal	Total	
Lower (bottom surface at center)	15 psi (Δp)	72	-148	636 w/ sif of 4.3	900
Upper (top surface at center)	15 psi (Δp)	72	+153	658 w/ sif of 4.3	900
Lower (outer rim)	Steady State Design Temp. of 1800 °F plus 15 psi (Δp)	1,450	--	2,181	900
Upper (outer rim)	Steady State Design Temp. of 1800 °F plus 15 psi (Δp)	1,227	--	3,350	900

For the 1,800 °F thermal loading, the structural evaluation indicates the need to refine the thermal design to raise the rim temperature of the tubesheet. However, the extent of the refinement indicated in Table 1 may be exaggerated as explained below. One of the conservatism in these results is the conservatism in the specification of a 15 psi differential pressure. Another significant conservatism in these results may be the specification of an 1,800 °F operating temperature which is greater than the expected operating temperature.

The greatest uncertainty in the structural evaluation of Table 1 is in the allowable stress. This uncertainty spans two issues. The first is the need to test material from the same process and batch as the tubesheets.

These tests need to be sufficient in number to build confidence in the material strength. The second issue concerns the extent to which the material can accommodate localized strain without failure. Thermal stresses are strain-controlled so that small strains in the local high stress region of the tubesheet may reduce the linearly-predicted stresses in Table 1 to acceptable values. This determination can only be made by testing.

FEATURE TESTS

It is important to note that a hot center with a cooler rim condition is evaluated experimentally by IF&P. The test setup for evaluating this prototypic condition is shown in Figure 10. As shown in this figure, a three-inch thick, 21.5 inch diameter test specimen plate (Fibroplate 2600 II) with 13 holes for filter candles is "sandwiched" between the upper and lower halves of a kiln. The bottom of the kiln contains the heating elements. The top of the kiln has a small vent for hot air to escape.

As shown in Figure 11, the bottom of the tubesheet is heated to 500 °F in one hour and held at 500 °F for about 1.5 hours. The temperature of the vent is 420° F and the outer edge of the tubesheet was "touchable" (perhaps < 140 °F). The temperature of the lower section is increased to 800 °F and held at 800 °F for more than an hour. At the 800 °F temperature condition, the temperature of the outer edge of the tubesheet is 205 °F as measured by a pyrometer. The kiln, with the tubesheet installed, is cooled to room temperature. A visual inspection did not reveal any cracks.

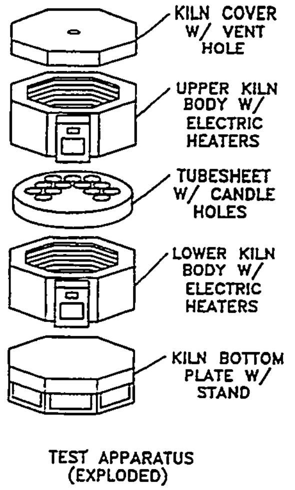

Figure 10 — Test Setup

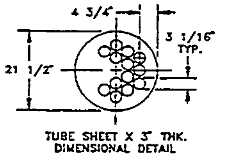

Test Specimen

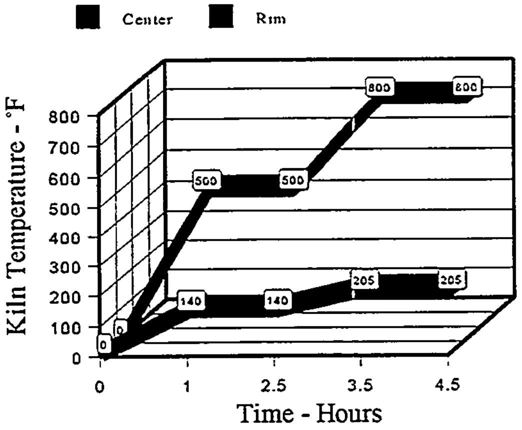

Figure 11 — Heating Histogram

In terms of a differential temperature, ΔT, between the gas and the outside diameter of the plate, this feature test is more severe (ΔT = 595 °F) than the maximum ΔT of 573 °F from the finite element analyses. From this observation, it would indicate that there may be crack resistive features or micro-crack type stress relieving mechanisms in the Fibroplate™ 2600 II ceramic material that have not been completely characterized in the material testing of coupon specimens. Coupon test specimens are used to establish the modulus of rupture and allowable stress limits for the material.

CONCLUSIONS

There is a need to refine the local insulation around the rim of the tubesheet examined in this investigation. The objective is to reduce the rim differential temperature down toward 110 °F.

It is important to perform feature testing of the ceramic tubesheet material such as performed by IF&P to establish the extent to which the material can accommodate localized stresses at the rim corners and at the ligaments between holes in the tubesheet.

The final design of a ceramic tubesheet should be confirmed by additional analysis of temperature transients to obtain guidance for operating limits.

A comprehensive material characterization program is needed for the Fibroplate™ 2600 II to establish the basic temperature dependent material properties needed in the finite element analysis and to establish a rational design criteria for this ceramic material.

The finite element analysis technology used in this investigation provides a powerful virtual prototyping capability to minimize the need for manufacturing actual components.

REFERENCES

1. ORNL/Sub/94-SR776V/01, “Thermal and Structural Design Analysis of a Ceramic Tubesheet”, November 22, 1996.

2. IF&P TR-001 "Ceramic Tubesheet Assembly Design Analysis Specification for the Power Systems Development Facility (PSDF) IF&P Filter Vessel", November 22, 1996.

3. Khonke, Peter, "ANSYS User's Manual, Theory Reference, Release 5.3", Report Number 000656, Seventh Edition, ANSYS, Inc., Houston, Pennsylvania, June 1996.